POLITECNICO DI TORINO
Repository ISTITUZIONALE

Experimental access to Transition Distribution Amplitudes with the PANDA experiment at FAIR

*Original*
Experimental access to Transition Distribution Amplitudes with the PANDA experiment at FAIR / The PANDA Collaboration, N., Singh, B.P., Erni, W., Keshelashvili, I., Krusche, B., Steinacher, M., Liu, B., Liu, H., Liu, Z., Shen, X., Wang, C., Zhao, J., Albrecht, M., Fink, M., Heinsius, F.H., Held, T., Holtmann, T., Koch, H., Kopf, B., Kümmel, M., et al.. - In: THE EUROPEAN PHYSICAL JOURNAL. A, HADRONS AND NUCLEI. - ISSN 1434-6001. - STAMPA. - 51:8(2015). [10.1140/epja/i2015-15107-y]

*Availability:*
This version is available at: 11583/2625751 since: 2015-12-15T20:28:06Z

*Publisher:*
Springer New York LLC

*Published*
DOI:10.1140/epja/i2015-15107-y

*Terms of use:*

This article is made available under terms and conditions as specified in the corresponding bibliographic description in the repository

*Publisher copyright*

(Article begins on next page)

26 November 2026

Eur. Phys. J. A (2015) **51**: 107
DOI 10.1140/epja/i2015-15107-y

**THE EUROPEAN PHYSICAL JOURNAL A**

Regular Article – Experimental Physics

# Experimental access to Transition Distribution Amplitudes with the $\bar{\text{P}}$ANDA experiment at FAIR

The $\bar{\text{P}}$ANDA Collaboration

B.P. Singh[1], W. Erni[2], I. Keshelashvili[2], B. Krusche[2], M. Steinacher[2], B. Liu[3], H. Liu[3], Z. Liu[3], X. Shen[3], C. Wang[3], J. Zhao[3], M. Albrecht[4], M. Fink[4], F.H. Heinsius[4], T. Held[4], T. Holtmann[4], H. Koch[4], B. Kopf[4], M. Kümmel[4], G. Kuhl[4], M. Kuhlmann[4], M. Leyhe[4], M. Mikirtychyants[4], P. Musiol[4], A. Mustafa[4], M. Pelizäus[4], J. Pychy[4], M. Richter[4], C. Schnier[4], T. Schröder[4], C. Sowa[4], M. Steinke[4], T. Triffterer[4], U. Wiedner[4], R. Beck[5], C. Hammann[5], D. Kaiser[5], B. Ketzer[5], M. Kube[5], P. Mahlberg[5], M. Rossbach[5], C. Schmidt[5], R. Schmitz[5], U. Thoma[5], D. Walther[5], C. Wendel[5], A. Wilson[5], A. Bianconi[6,57], M. Bragadireanu[7], M. Caprini[7], D. Pantea[7], D. Pietreanu[7], M.E. Vasile[7], B. Patel[8], D. Kaplan[9], P. Brandys[10], T. Czyzewski[10], W. Czyzycki[10], M. Domagala[10], M. Hawryluk[10], G. Filo[10], M. Krawczyk[10], D. Kwiatkowski[10], E. Lisowski[10], F. Lisowski[10], T. Fiutowski[11], M. Idzik[11], B. Mindur[11], D. Przyborowski[11], K. Swientek[11], B. Czech[12], S. Kliczewski[12], K. Korcyl[12], A. Kozela[12], P. Kulessa[12], P. Lebiedowicz[12], K. Malgorzata[12], K. Pysz[12], W. Schäfer[12], R. Siudak[12], A. Szczurek[12], J. Biernat[13], S. Jowzaee[13], B. Kamys[13], S. Kistryn[13], G. Korcyl[13], W. Krzemien[13], A. Magiera[13], P. Moskal[13], M. Palka[13], A. Psyzniak[13], Z. Rudy[13], P. Salabura[13], J. Smyrski[13], P. Strzempek[13], A. Wrońska[13], I. Augustin[14], I. Lehmann[14], D. Nicmorus[14], G. Schepers[14], L. Schmitt[14], M. Al-Turany[15], U. Cahit[15], L. Capozza[15], A. Dbeyssi[15], H. Deppe[15], R. Dzhygadlo[15], A. Ehret[15], H. Flemming[15], A. Gerhardt[15], K. Götzen[15], R. Karabowicz[15], R. Kliemt[15], J. Kunkel[15], U. Kurilla[15], D. Lehmann[15], J. Lühning[15], F. Maas[15], C. Morales Morales[15], M.C. Mora Espí[15], F. Nerling[15], H. Orth[15], K. Peters[15], D. Rodríguez Piñeiro[15], N. Saito[15], T. Saito[15], A. Sánchez Lorente[15], C.J. Schmidt[15], C. Schwarz[15], J.Schwiening[15], M. Traxler[15], R. Valente[15], B. Voss[15], P. Wieczorek[15], A. Wilms[15], M. Zühlsdorf[15], V.M. Abazov[16], G. Alexeev[16], A. Arefiev[16], V.I. Astakhov[16], M.Yu. Barabanov[16], B.V. Batyunya[16], Yu.I. Davydov[16], V.Kh. Dodokhov[16], A.A. Efremov[16], A.G. Fedunov[16], A.A. Festchenko[16], A.S. Galoyan[16], S. Grigoryan[16], A. Karmokov[16], E.K. Koshurnikov[16], V.I. Lobanov[16], Yu.Yu. Lobanov[16], A.F. Makarov[16], L.V. Malinina[16], V.L. Malyshev[16], G.A. Mustafaev[16], A. Olshevskiy[16], M.A. Pasyuk[16], E.A. Perevalova[16], A.A. Piskun[16], T.A. Pocheptsov[16], G. Pontecorvo[16], V.K. Rodionov[16], Yu.N. Rogov[16], R.A. Salmin[16], A.G. Samartsev[16], M.G. Sapozhnikov[16], G.S. Shabratova[16], N.B. Skachkov[16], A.N. Skachkova[16], E.A. Strokovsky[16], M.K. Suleimanov[16], R.Sh. Teshev[16], V.V. Tokmenin[16], V.V. Uzhinsky[16], A.S. Vodopyanov[16], S.A. Zaporozhets[16], N.I. Zhuravlev[16], A.G. Zorin[16], D. Branford[17], D. Glazier[17], D. Watts[17], P. Woods[17], A. Britting[18], W. Eyrich[18], A. Lehmann[18], F. Uhlig[18], S. Dobbs[19], K. Seth[19], A. Tomaradze[19], T. Xiao[19], D. Bettoni[20], V. Carassiti[20], A. Cotta Ramusino[20], P. Dalpiaz[20], A. Drago[20], E. Fioravanti[20], I. Garzia[20], M. Savriè[20], G. Stancari[20], V. Akishina[21], I. Kisel[21], I. Kulakov[21], M. Zyzak[21], R. Arora[22], T. Bel[22], A. Gromliuk[22], G. Kalicy[22], M. Krebs[22], M. Patsyuk[22], M. Zuehlsdorf[22], N. Bianchi[23], P. Gianotti[23], C. Guaraldo[23], V. Lucherini[23], E. Pace[23], A. Bersani[24], G. Bracco[24], M. Macri[24], R.F. Parodi[24], S. Bianco[25], D. Bremer[25], K.T. Brinkmann[25], S. Diehl[25], V. Dormenev[25], P. Drexler[25], M. Düren[25], T. Eissner[25], E. Etzelmüller[25], K. Föhl[25], M. Galuska[25], T. Gessler[25], E. Gutz[25], A. Hayrapetyan[25], J. Hu[25], B. Kröck[25], W. Kühn[25], T. Kuske[25], S. Lange[25], Y. Liang[25], O. Merle[25], V. Metag[25], D. Mülhheim[25], D. Münchow[25], M. Nanova[25], R. Novotny[25], A. Pitka[25], T. Quagli[25], J. Rieke[25], C. Rosenbaum[25], R. Schnell[25], B. Spruck[25], H. Stenzel[25], U. Thöring[25], M. Ullrich[25], T. Wasem[25], M. Werner[25], H.G. Zaunick[25], D. Ireland[26], G. Rosner[26], B. Seitz[26], P.N. Deepak[27], A.V. Kulkarni[27], A. Apostolou[28], M. Babai[28], M. Kavatsyuk[28], P. Lemmens[28], M. Lindemulder[28], H. Löhner[28], J. Messchendorp[28], P. Schakel[28], H. Smit[28], J.C. van der Weele[28], M. Tiemens[28], R. Veenstra[28], S. Vejdani[28], K. Kalita[29], D.P. Mohanta[29], A. Kumar[30], A. Roy[30], R. Sahoo[30], H. Sohlbach[31], M. Büscher[32], L. Cao[32], A. Cebulla[32], D. Deermann[32], R. Dosdall[32], S. Esch[32], I. Georgadze[32], A. Gillitzer[32], A. Goerres[32], F. Goldenbaum[32], D. Grunwald[32], A. Herten[32], Q. Hu[32], G. Kemmerling[32], H. Kleines[32], V. Kozlov[32], A. Lehrach[32], S. Leiber[32], R. Maier[32], R. Nellen[32], H. Ohm[32], S. Orfanitski[32], D. Prasuhn[32], E. Prencipe[32], J. Ritman[32], S. Schadmand[32], J. Schumann[32], T. Sefzick[32], V. Serdyuk[32], G. Sterzenbach[32], T. Stockmanns[32], P. Wintz[32], P. Wüstner[32], H. Xu[32], S. Li[33], Z. Li[33], Z. Sun[33], H. Xu[33], V. Rigato[34], S. Fissum[35], K. Hansen[35], L. Isaksson[35], M. Lundin[35], B. Schröder[35], P. Achenbach[36], S. Bleser[36], M. Cardinali[36], O. Corell[36], M. Deiseroth[36], A. Denig[36], M. Distler[36], F. Feldbauer[36], M. Fritsch[36], P. Jasinski[36], M. Hoek[36], D. Kangh[36], A. Karavdina[36], W. Lauth[36], H. Leithoff[36], H. Merkel[36], M. Michel[36], C. Motzko[36], U. Müller[36], O. Noll[36], S. Plueger[36], J. Pochodzalla[36], S. Sanchez[36], S. Schlimme[36], C. Sfienti[36], M. Steinen[36], M. Thiel[36], T. Weber[36],

M. Zambrana[36,a], V.I. Dormenev[37], A.A. Fedorov[37], M.V. Korzihik[37], O.V. Missevitch[37], P. Balanutsa[38], V. Balanutsa[38], V. Chernetsky[38], A. Demekhin[38], A. Dolgolenko[38], P. Fedorets[38], A. Gerasimov[38], V. Goryachev[38], V. Varentsov[38], A. Boukharov[39], O. Malyshev[39], I. Marishev[39], A. Semenov[39], I. Konorov[40], S. Paul[40], S. Grieser[41], A.K. Hergemöller[41], A. Khoukaz[41], E. Köhler[41], A. Täschner[41], J. Wessels[41], S. Dash[42], M. Jadhav[42], S. Kumar[42], P. Sarin[42], R. Varma[42], V.B. Chandratre[43], V. Datar[43], D. Dutta[43], V. Jha[43], H. Kumawat[43], A.K. Mohanty[43], B. Roy[43], Y. Yan[44], K. Chinorat[44], K. Khanchai[44], L. Ayut[44], S. Pornrad[44], A.Y. Barnyakov[45], A.E. Blinov[45], V.E. Blinov[45,46], V.S. Bobrovnikov[45], S.A. Kononov[45,47], E.A. Kravchenko[45,47], I.A. Kuyanov[45], A.P. Onuchin[45,46], A.A. Sokolov[45,47], Y.A. Tikhonov[45,47], E. Atomssa[48], T. Hennino[48], M. Imre[48], R. Kunne[48], C. Le Galliard[48], B. Ma[48], D. Marchand[48], S. Ong[48], B. Ramstein[48], P. Rosier[48], E. Tomasi-Gustafsson[48], J. Van de Wiele[48], G. Boca[49], S. Costanza[49], P. Genova[49], L. Lavezzi[49], P. Montagna[49], A. Rotondi[49], V. Abramov[50], N. Belikov[50], S. Bukreeva[50], A. Davidenko[50], A. Derevschikov[50], Y. Goncharenko[50], V. Grishin[50], V. Kachanov[50], V. Kormilitsin[50], Y. Melnik[50], A. Levin[50], N. Minaev[50], V. Mochalov[50], D. Morozov[50], L. Nogach[50], S. Poslavskiy[50], A. Ryazantsev[50], S. Ryzhikov[50], P. Semenov[50], I. Shein[50], A. Uzunian[50], A. Vasiliev[50], A. Yakutin[50], B. Yabsley[51], T. Bäck[52], B. Cederwall[52], K. Makónyi[53], P.E. Tegnér[53], K.M. von Würtemberg[53], S. Belostotski[54], G. Gavrilov[54], A. Izotov[54], A. Kashchuk[54], O. Levitskaya[54], S. Manaenkov[54], O. Miklukho[54], Y. Naryshkin[54], K. Suvorov[54], D. Veretennikov[54], A. Zhadanov[54], A.K. Rai[55], S.S. Godre[56], R. Duchat[56], A. Amoroso[57], M.P. Bussa[57], L. Busso[57], F. De Mori[57], M. Destefanis[57], L. Fava[57], L. Ferrero[57], M. Greco[57], M. Maggiora[57], G. Maniscalco[57], S. Marcello[57], S. Sosio[57], S. Spataro[57], L. Zotti[57], D. Calvo[58], S. Coli[58], P. De Remigis[58], A. Filippi[58], G. Giraudo[58], S. Lusso[58], G. Mazza[58], M. Mingnore[58], A. Rivetti[58], R. Wheadon[58], F. Balestra[59], F. Iazzi[59], R. Introzzi[59], A. Lavagno[59], H. Younis[59], R. Birsa[60], F. Bradamante[60], A. Bressan[60], A. Martin[60], H. Clement[61], B. Gålnander[62], L. Caldeira Balkeståhl[63], H. Calén[63], K. Fransson[63], T. Johansson[63], A. Kupsc[63], P. Marciniewski[63], J. Pettersson[63], K. Schönning[63], M. Wolke[63], J. Zlomanczuk[63], J. Díaz[64], A. Ortiz[64], P.C. Vinodkumar[65], A. Parmar[65], A. Chlopik[66], D. Melnychuk[66], B. Slowinski[66], A. Trzcinski[66], M. Wojciechowski[66], S. Wronka[66], B. Zwieglinski[66], P. Bühler[67], J. Marton[67], K. Suzuki[67], E. Widmann[67], J. Zmeskal[67]
and
B. Fröhlich[15], D. Khaneft[15], D. Lin[15], I. Zimmermann[15], and K. Semenov-Tian-Shansky[68]

[1] Aligarth Muslim University, Physics Department, Aligarth, India
[2] Universität Basel, Switzerland
[3] Institute of High Energy Physics, Chinese Academy of Sciences, Beijing, China
[4] Universität Bochum I. Institut für Experimentalphysik, Germany
[5] Rheinische Friedrich-Wilhelms-Universität Bonn, Germany
[6] Università di Brescia, Italy
[7] Institutul National de C&D pentru Fizica si Inginerie Nucleara “Horia Hulubei”, Bukarest-Magurele, Romania
[8] P.D. Patel Institute of Applied Science, Department of Physical Sciences, Changa, India
[9] IIT, Illinois Institute of Technology, Chicago, USA
[10] University of Technology, Institute of Applied Informatics, Cracow, Poland
[11] AGH, University of Science and Technology, Cracow, Poland
[12] IFJ, Institute of Nuclear Physics PAN, Cracow, Poland
[13] Instytut Fizyki, Uniwersytet Jagiellonski, Cracow, Poland
[14] FAIR, Facility for Antiproton and Ion Research in Europe, Darmstadt, Germany
[15] GSI Helmholtzzentrum für Schwerionenforschung GmbH, Darmstadt, Germany
[16] Veksler-Baldin Laboratory of High Energies (VBLHE), Joint Institute for Nuclear Research, Dubna, Russia
[17] University of Edinburgh, UK
[18] Friedrich Alexander Universität Erlangen-Nürnberg, Germany
[19] Northwestern University, Evanston, USA
[20] Università di Ferrara and INFN Sezione di Ferrara, Ferrara, Italy
[21] Frankfurt Institute for Advanced Studies, Frankfurt, Germany
[22] Goethe Universität, Institut für Kernphysik, Frankfurt, Germany
[23] INFN, Laboratori Nazionali di Frascati, Italy
[24] INFN, Sezione di Genova, Italy
[25] Justus Liebig-Universität Gießen II. Physikalisches Institut, Germany
[26] University of Glasgow, UK
[27] Birla Institute of Technology and Science - Pilani, K.K. Birla Goa Campus, Goa, India
[28] University of Groningen, KVI - Center for Advanced Radiation Technology, Groningen, The Netherlands
[29] Gauhati University, Physics Department, Guwahati, India
[30] Indian Institute of Technology Indore, School of Science, Indore, India
[31] Fachhochschule Südwestfalen Iserlohn, Germany
[32] Forschungszentrum Jülich, Institut für Kernphysik, Jülich, Germany
[33] Chinese Academy of Science, Institute of Modern Physics, Lanzhou, China

[a] e-mail: zambrana@kph.uni-mainz.de

[34] INFN Laboratori Nazionali di Legnaro, Italy
[35] Lunds Universitet, Department of Physics, Lund, Sweden
[36] Johannes Gutenberg-Universität, Institut für Kernphysik, Mainz, Germany
[37] Research Institute for Nuclear Problems, Belarus State University, Minsk, Belarus
[38] Institute for Theoretical and Experimental Physics, Moscow, Russia
[39] Moscow Power Engineering Institute, Moscow, Russia
[40] Technische Universität München, Germany
[41] Westfälische Wilhelms-Universität Münster, Germany
[42] Indian Institute of Technology Bombay, Department of Physics, Mumbai, India
[43] Nuclear Physics Division, Bhabha Atomic Research Centre, Mumbai, India
[44] Suranaree University of Technology, Nakhon Ratchasima, Thailand
[45] Budker Institute of Nuclear Physics of Russian Academy of Science, Novosibirsk, Russia
[46] Novosibirsk State Technical University, Novosibirsk, Russia
[47] Novosibirsk State University, Novosibirsk, Russia
[48] Institut de Physique Nucléaire d'Orsay (UMR8608), CNRS/IN2P3 and Université Paris-Sud, Orsay, France
[49] Dipartimento di Fisica, Università di Pavia, INFN Sezione di Pavia, Pavia, Italy
[50] Institute for High Energy Physics, Protvino, Russia
[51] University of Sidney, School of Physics, Sidney, Australia
[52] Kungliga Tekniska Högskolan, Stockholm, Sweden
[53] Stockholms Universitet, Stockholm, Sweden
[54] Petersburg Nuclear Physics Institute of Russian Academy of Science, Gatchina, St. Petersburg, Russia
[55] Sardar Vallabhbhai National Institute of Technology, Applied Physics Department, Surat, India
[56] Veer Narmand South Gujarat University, Department of Physics, Surat, India
[57] Università di Torino and INFN Sezione di Torino, Torino, Italy
[58] INFN, Sezione di Torino, Torino, Italy
[59] Politecnico di Torino and INFN Sezione di Torino, Torino, Italy
[60] Università di Trieste and INFN Sezione di Trieste, Trieste, Italy
[61] Universität Tübingen, Tübingen, Germany
[62] The Svedberg Laboratory, Uppsala, Sweden
[63] Uppsala Universitet, Institutionen för Strålningsvetenskap, Uppsala, Sweden
[64] Instituto de Física Corpuscular (IFIC) Universidad de Valencia - CSIC, Paterna, Valencia, Spain
[65] Sardar Patel University, Physics Department, Vallabh Vidynagar, India
[66] National Centre for Nuclear Research, Warsaw, Poland
[67] Österreichische Akademie der Wissenschaften, Stefan Meyer Institut für Subatomare Physik, Wien, Austria
[68] IFPA, département AGO, Université de Liège, Liège, Belgium

Received: 4 September 2014 / Revised: 21 May 2015
Published online: 28 August 2015
© The Author(s) 2015. This article is published with open access at Springerlink.com
Communicated by P. Rossi

**Abstract.** Baryon-to-meson Transition Distribution Amplitudes (TDAs) encoding valuable new information on hadron structure appear as building blocks in the collinear factorized description for several types of hard exclusive reactions. In this paper, we address the possibility of accessing nucleon-to-pion ($\pi N$) TDAs from $\bar{p}p \to e^+e^-\pi^0$ reaction with the future $\bar{\mathrm{P}}$ANDA detector at the FAIR facility. At high center-of-mass energy and high invariant mass squared of the lepton pair $q^2$, the amplitude of the signal channel $\bar{p}p \to e^+e^-\pi^0$ admits a QCD factorized description in terms of $\pi N$ TDAs and nucleon Distribution Amplitudes (DAs) in the forward and backward kinematic regimes. Assuming the validity of this factorized description, we perform feasibility studies for measuring $\bar{p}p \to e^+e^-\pi^0$ with the $\bar{\mathrm{P}}$ANDA detector. Detailed simulations on signal reconstruction efficiency as well as on rejection of the most severe background channel, *i.e.* $\bar{p}p \to \pi^+\pi^-\pi^0$ were performed for the center-of-mass energy squared $s = 5\,\mathrm{GeV}^2$ and $s = 10\,\mathrm{GeV}^2$, in the kinematic regions $3.0 < q^2 < 4.3\,\mathrm{GeV}^2$ and $5 < q^2 < 9\,\mathrm{GeV}^2$, respectively, with a neutral pion scattered in the forward or backward cone $|\cos\theta_{\pi^0}| > 0.5$ in the proton-antiproton center-of-mass frame. Results of the simulation show that the particle identification capabilities of the $\bar{\mathrm{P}}$ANDA detector will allow to achieve a background rejection factor of $5 \cdot 10^7$ ($1 \cdot 10^7$) at low (high) $q^2$ for $s = 5\,\mathrm{GeV}^2$, and of $1 \cdot 10^8$ ($6 \cdot 10^6$) at low (high) $q^2$ for $s = 10\,\mathrm{GeV}^2$, while keeping the signal reconstruction efficiency at around 40%. At both energies, a clean lepton signal can be reconstructed with the expected statistics corresponding to $2\,\mathrm{fb}^{-1}$ of integrated luminosity. The cross sections obtained from the simulations are used to show that a test of QCD collinear factorization can be done at the lowest order by measuring scaling laws and angular distributions. The future measurement of the signal channel cross section with $\bar{\mathrm{P}}$ANDA will provide a new test of the perturbative QCD description of a novel class of hard exclusive reactions and will open the possibility of experimentally accessing $\pi N$ TDAs.

## 1 Introduction

Studies of hard exclusive reactions, such as Deeply Virtual Compton Scattering (DVCS) and Hard Exclusive Meson Electroproduction, within the collinear factorization approach, allow to challenge a QCD-based description of hadron structure (for a review see *e.g.* [1]). By separating the hard and soft stages of the interaction, at high energies the amplitudes of these reactions can be presented in the form of convolutions of hard parts, computable in perturbation theory, and soft parts: generalized parton distributions (GPDs) and meson distribution amplitudes (DAs). These non-perturbative objects can be assigned a rigorous meaning in QCD and allow to interpret hadronic structural information in terms of quark and gluon degrees of freedom. Along with the usual parton distribution functions (PDFs) and form factors (FFs), GPDs encode valuable structural information about hadrons. In particular, GPDs are currently seen as a tool to study the nature and origin of the nucleon spin. Moreover, GPDs allow an extremely vivid interpretation in the impact parameter space as spatial femto-photographs of the hadron interior in the transverse plane.

Further development of the GPD approach led to the introduction of baryon-to-meson transition distribution amplitudes (TDAs) [2,3] broadening the class of hard reactions for which a factorized description of the scattering amplitudes for strong interaction phenomena can be applied. The physical picture encoded in baryon-to-meson TDAs is conceptually close to that contained in baryon GPDs and baryon DAs. Baryon-to-meson TDAs probe partonic correlations between states of different baryonic charge thus giving access to non-minimal Fock components of baryon light-cone wave functions. Fourier transforming TDAs to the impact parameter space allows one to perform femto-photography of hadrons from a new perspective. In particular, nucleon-to-pion ($\pi N$) TDAs may be used as a tool for spatial imaging of the structure of the pion cloud inside the nucleon. This opens a new window for the investigation of the various facets of the nucleon internal structure. A dedicated program for accessing $\pi N$ TDAs in the space-like regime through backward pion electroproduction [4,5] was proposed for JLab Hall B @ 12 GeV (see ref. [6] for preliminary studies dedicated to JLab @ 6 GeV).

The future PANDA (antiProton ANnihilations at DArmstadt) experiment at FAIR (Facility for Antiproton and Ion Research) operating a high-intensity antiproton beam with momentum up to 15 GeV offers unique possibilities for new investigations of the hadron structure (see refs. [7,8]) complementing the results obtained from the studies of lepton beam induced reactions. In particular, the PANDA experimental program includes dedicated measurements of the time-like electromagnetic form factors of the proton, mainly through the annihilation process $\bar{p}p \to e^+e^-$, for which feasibility studies with the PANDA detector have already been performed at several antiproton beam energies [9]. The high intensity of the antiproton beam, together with the performance of the PANDA detector, including particle identification capabilities, will render an unprecedent accuracy in the measurements over a large range of four-momentum transfer squared, as shown by the simulations.

Outside the resonance region (*i.e.* for sufficiently high invariant mass of the lepton pair) the nucleon electromagnetic form factors admit a factorized description within the perturbative QCD (pQCD) approach and follow a scaling law [10,11]. This framework was further developed in [3,12] and was employed in [13–15] to provide a factorized description of nucleon-antinucleon annihilation into a highly virtual lepton pair and a pion in terms of $\pi N$ TDAs and nucleon DAs. Note that a similar treatment can be applied to the scattering amplitude, when the lepton pair originates from a heavy charmonium state [16–18]. At lower energies, where factorization does not hold, descriptions of the $\bar{p}p \to e^+e^-\pi^0$ amplitude in terms of a one-nucleon-exchange model and the Regge theory [19,20] have been proposed, and preliminary studies of the cross section measurement with PANDA have already been performed [21].

Thus, alongside with the time-like electromagnetic form factor measurements, it is extremely appealing to test the predictions of the pQCD collinear factorized description of $\bar{p}p \to e^+e^-\pi^0$ and address the possibility of accessing the proton/antiproton-to-pion TDAs with the PANDA detector through the measurement of the corresponding differential cross section.

In the present paper we consider the feasibility of measuring the $\bar{p}p \to e^+e^-\pi^0$ signal channel cross sections at high center-of-mass energy and high four-momentum squared of the virtual photon, with the produced $\pi^0$ scattered into the forward or backward angular regions, in which the factorization theorem is expected to be valid [22]. Proton-antiproton annihilation into three pions, *i.e.* $\bar{p}p \to \pi^+\pi^-\pi^0$, appears as the most severe background channel for the process of interest, as it contains the same number of particles in the final state, with identical charge signature. Detailed simulations have been performed on the signal reconstruction efficiency and on the background rejection. The feasibility of the measurement has been studied using an integrated luminosity of $2\,\mathrm{fb}^{-1}$. The cross sections obtained from the simulations are used to test pQCD at the lowest order by measuring scaling laws and angular distributions.

## 2 Set-up of the future PANDA experiment

An extensive description of the PANDA detector can be found in ref. [7]. Here we give a brief outline of the main components which are relevant to this analysis.

A High Energy Storage Ring (HESR), in which both stochastic and electron cooling systems are foreseen, will provide a high quality antiproton beam of momentum between 1.5 and 15 GeV. The concept of the detector, the read out and the data acquisition system are similar to that of other recently built detectors, such as ATLAS, CMS, COMPASS and BaBar. However, the high expected rate of $2 \cdot 10^7$ interactions per second and the multipurpose character of the detector, including the measurement

of low cross sections in the charm sector, demand unique detection capabilities in $\bar{\text{P}}$ANDA. These include geometrical acceptance of almost $4\pi$, energy and momentum resolutions at the level of a few percent, fast data acquisition and high radiation hardness. In the HESR high-luminosity mode, the average design luminosity of $\mathcal{L} = 1.5 \cdot 10^{32}\,\text{cm}^{-2}\,\text{s}^{-1}$ will be reached with a pellet target of thickness $4 \cdot 10^{15}$ hydrogen atoms/cm$^2$, and $10^{11}$ stored antiprotons in HESR. The detector is divided in a target spectrometer, in which the target is surrounded by a solenoid magnet providing up to 2 T magnetic field, and a forward spectrometer, based on a 2 Tm dipole magnet, to ensure particle detection at small polar angles, down to 2°. Tracking, particle identification, electromagnetic calorimetry, and muon identification detectors are designed for both spectrometers. The reconstruction of the interaction point as well as secondary vertices is done with the microvertex detector (MVD). The concept of the MVD is based on radiation hard silicon pixel detectors with fast individual pixel readout circuits and silicon strip detectors, making a four layer barrel detector with an inner radius of 2.5 cm and an outer radius of 13 cm. The charged particle tracking and identification is provided by the straw tube tracker (STT), consisting of aluminized mylar tubes called "straws", arranged in planar layers and mounted around the MVD in a total of 24 layers. Of these, the 8 central ones are tilted to achieve a resolution of 3 mm also in the direction parallel to the beam. Track detection at angles below 22° (not fully covered by the STT) is completed by three chambers of gas electron multiplier (GEM) detectors placed 1.1 m, 1.4 m and 1.9 m downstream of the target. The chambers are designed to sustain a high counting rate of particles peaked at the most forward angles due to the relativistic boost of the reaction products. Additional components are required for the identification of hadrons and leptons in a wide kinematic range. For slow particles at large polar angles, particle identification will be provided by the time-of-flight (TOF) detector, with time resolution between 50 and 100 ps as required by the 50–100 cm of flight path in the target spectrometer. The $PbWO_4$ electromagnetic calorimeter (EMC), operated at −25 °C, is designed for the detection of photons and electrons. Here, the fast scintillator material with short radiation length is required by the expected high counting rates and geometrically compact design of the target spectrometer. Crystals of 20 cm length, *i.e.* approximately 22 radiation lengths, are used in order to achieve an energy resolution below 2% at 1 GeV. For the efficient separation of pions from electrons at momenta $p < 1\,\text{GeV}$, a barrel and a forward disk DIRC (detection of internally reflected Cherenkov light) complete the particle identification (PID) system.

## 3 PANDA detector reconstruction capabilities

In the physics analysis, the generated events by the Monte Carlo programs (corresponding to signal or background channels) are, in a first step, passed through a full simulation of the $\bar{\text{P}}$ANDA detector, based on the GEANT 4 package [23], which takes care of the propagation of particles through the detector. Hit and energy loss information is then digitized according to a model simulating electronic properties, including electronic noise, yielding a response of the different detectors. The second step is the reconstruction of the relevant physical quantities for the identification of electrons, such as momentum, ratio of energy loss to path length $\text{d}E/\text{d}x$ in the STT, Cherenkov angle in the DIRC detectors, and energy deposit in the EMC from the simulated data. These two steps have been described in detail in ref. [7], so we will give here only the main features which are relevant for the electron and photon identification.

The truncated arithmetic mean method is used on the $\text{d}E/\text{d}x$ values for particle identification in order to exclude from the sample the largest values which correspond to the extended Landau tail of the distribution. The value used for the calculation of the arithmetic mean corresponds to 70% of the $N$ individual $\text{d}E/\text{d}x$ values. In this way a compromise between the requirements of the best resolution, defined through the width of a Gaussian fit, and the smallest tail of the distribution is achieved. A resolution of $< 10\%$ in $\text{d}E/\text{d}x$ is obtained for pions of momentum 1 GeV, which corresponds on average to four standard deviations of the distance between the truncated means for electrons and pions.

For the DIRC detector, the Cherenkov angle is given with a resolution $\sigma_C = \sigma_{C,\gamma}/\sqrt{N_{ph}}$, where the single photon resolution is $\sigma_{C,\gamma} = 10\,\text{mrad}$. The number of detected photons, $N_{ph}$, has a dependence on the velocity and path length of the particle travelling inside the Cherenkov radiator. To calculate the Cherenkov angle, the software takes also into account the quantum efficiency of the photodectectors and the transmission and reflectivity losses in the detector material. A resolution of 2.3 mrad is obtained for pions of momentum 1 GeV [24]. The DIRC discrimination power is higher at lower energies due to the larger difference between the Cherenkov angles for pions and electrons: at momentum 500 MeV the difference in the angles for the Cherenkov light amounts to 36 mrad whereas at momentum 1.5 GeV it is 4 mrad.

The most important detector for electron identification is the electromagnetic calorimeter. Electron identification is done using the ratio $E/p$ between the measured energy deposit $E$ and the reconstructed momentum $p$. In the electromagnetic calorimeter, the electrons deposit all (up to minor losses due to dead material, crystal edges, etc.) their energy via an electromagnetic shower, whereas muons and hadrons loose only a much lower fraction of their energy via Bethe-Bloch excitations and ionization processes. However, there could be cases in which a high energy deposit would be the consequence of hadronic interactions. In those cases the analysis of the shower shape plays an important role in the particle identification process. The Molière radius of $PbWO_4$ is 2 cm and it is of the order of the crystal front size dimensions, $2.1 \times 2.1\,\text{cm}^2$ in the barrel and backward endcap and $2.44 \times 2.44\,\text{cm}^2$ in the forward endcap of the calorimeter. In the case of an electromagnetic shower the largest fraction of the energy

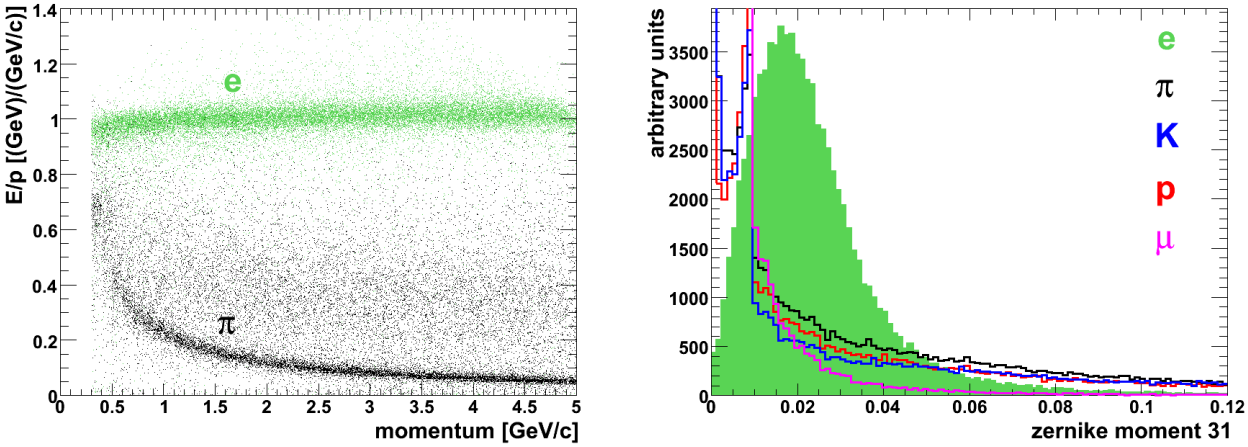


**Fig. 1.** The ratio $E/p$ between the measured energy deposit $E$ and the reconstructed momentum $p$ for an electron sample and for a pion sample (left) and the distribution of the Zernike moment 31 for samples of different particle species (right). The figures are taken from refs. [7,9].

deposition is contained in a few crystals, whereas in the case of a hadronic interaction, the energy deposition will be distributed in a larger volume. The shower shape analysis uses the energy deposited in the central crystal of the cluster relative to that in the $3 \times 3$ or $5 \times 5$ crystal arrays surrounding it. The ratio between these two numbers is a measure for the cluster size and shape, and therefore it is an indicator for an electromagnetic or a hadronic interaction. In addition, a set of four Zernike moments[1] are used to describe the spatial distribution of the energy within the shower by using polynomials in the radial and angular coordinates. Figure 1 shows two examples on how $E/p$ and one of the Zernike moments can be used to discriminate electrons from pions (for an extensive description, see ref. [7], chapt. 3, subsect. 3.3.3).

Probabilities for the identification of a given particle using different hypotheses (electron, muon, pion, kaon and proton) are calculated on the basis of the results given by simulations using these species as input for the event generators for an extended range of momenta and polar angles. In addition to the variables discussed above, $\mathrm{d}E/\mathrm{d}x$ information from the microvertex detector as well as hit information from the muon detector are included. In the case of the electromagnetic calorimeter, this probability is calculated using the output of a neural network which uses as the input the list of shower shape and Zernike parameters for a cluster described previously, as discussed in [7]. A global particle identification likelihood can be calculated using the individual subdetector likelihoods. Depending on the signal and background channels, the cuts for the particle identification can be adjusted to get the best signal efficiency for the required background suppression.

[1] The Zernike polynomials are a complete orthogonal set in the unit disk $0 < x^2 + y^2 < 1$. The projections of a function $f(x, y)$ on the basis of the Zernike polynomials are called the Zernike moments of $f$. Details can be found, for instance, in ref. [25], chapt. 9, sect. 2.

In this analysis we use a number of simplifications with respect to the continuously developing $\bar{\mathrm{P}}$ANDA framework. Charged particle tracking was performed without pattern recognition, leading to an overestimation of the track finding efficiency compared to the performance studies summarized in ref. [26]. The Kalman filter for track fitting used a less refined material distribution. For the Cherenkov angle, photon transport and photon detection was not simulated, but instead a smearing technique was applied. For the description of the electromagnetic showers GEANT 4.7 was used, for which deviations to data were reported by the BaBar experiment [27].

## 4 Theoretical overview and event generation

In this section we present a short overview of the basic definitions and conventions employed for the factorized description of the nucleon-antinucleon annihilation into a high invariant mass lepton pair in association with a $\pi^0$ meson. The details can be found in refs. [13–15].

To the leading order in the electromagnetic coupling the reaction proceeds in two stages: firstly proton and antiproton annihilate to produce a virtual photon and a neutral pion and subsequently the virtual photon decays into the lepton pair:

$$\begin{aligned} \bar{p}(p_1, s_1) + p(p_2, s_2) &\to \gamma^*(q) + \pi^0(k_3) \\ &\to e^+(k_1) + e^-(k_2) + \pi^0(k_3), \end{aligned} \quad (1)$$

where by $s_{1,2}$ we denote the antinucleon and nucleon spin variables.

According to the usual $\bar{\mathrm{P}}$ANDA conventions, we choose the $z$ axis along the colliding $\bar{p}p$ with the positive direction along the antinucleon beam. The two remaining spatial directions are referred to as the transverse plane. In order to specify the two kinematic regimes subject to the factorized description in terms of $\pi N$ TDAs we switch to the

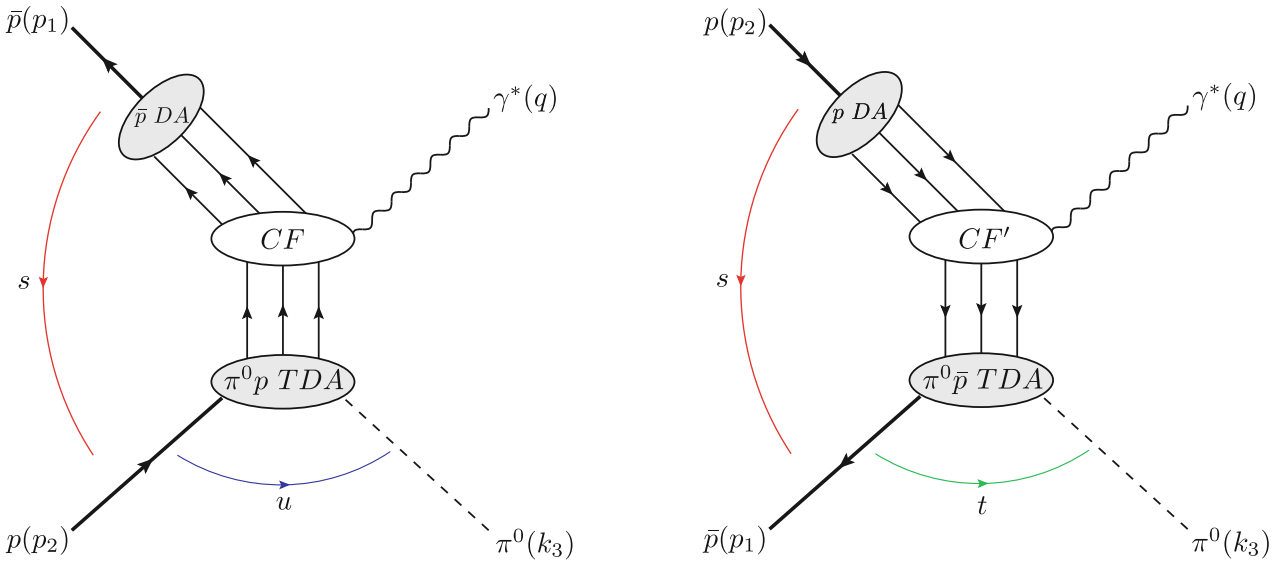


**Fig. 2.** The two possibilities for factorization in the annihilation process $\bar{p}p \to \gamma^*\pi_0$, for both kinematics: backwards (left) and forward (right). $\bar{p}$ ($p$) DA stands for the distribution amplitude of antiproton (proton). $\pi^0 p$ ($\pi^0\bar{p}$) TDA stands for the transition distribution amplitude from a proton (antiproton) to a neutral pion. $CF$ and $CF'$ stand for coefficient functions (hard subprocess amplitudes).

light-cone variables and introduce the $t$- and $u$-channel light-cone vectors $n^t$, $p^t$; $n^u$, $p^u$ ($p^2 = n^2 = 0$, $2p\cdot n = 1$). To quantify the longitudinal momentum transfers in the appropriate channels we define the $t$- and $u$-channel skewness variables

$$\xi^t \equiv -\frac{(k_3 - p_1)\cdot n^t}{(k_3 + p_1)\cdot n^t} \quad \xi^u \equiv -\frac{(k_3 - p_2)\cdot n^u}{(k_3 + p_2)\cdot n^u}\,. \tag{2}$$

The factorization mechanism suggested in [13] for the $\bar{p}(p_1) + p(p_2) \to \gamma^*(q) + \pi^0(k_3)$ subprocess of the reaction (1) is schematically depicted on fig. 2. The amplitude is presented as a convolution of the hard part computed by means of perturbative QCD with nucleon DAs and nucleon-to-pion TDAs encoding the soft dynamics. The factorization is assumed to be achieved in two distinct kinematic regimes:

- The near forward regime ($s = (p_1+p_2)^2$, $q^2$ - large with $\xi^t$ fixed; and $|t| = |(k_3 - p_1)^2| \sim 0$); it corresponds to the produced pion moving nearly in the direction of the initial $\bar{p}$ in the $\bar{p}p$ center-of-mass (CM) system.
- The near backward regime ($s = (p_1 + p_2)^2$, $q^2$ - large with $\xi^u$ fixed; and $|u| = |(k_3 - p_2)^2| \sim 0$); it corresponds to the produced pion moving nearly in the direction of the initial $p$ in $\bar{p}p$ CM system.

The suggested reaction mechanism should manifest itself through the distinctive forward and backward peaks of the $\bar{p}p \to \gamma^*\pi^0$ cross section. The charge conjugation invariance results in the perfect symmetry between the two kinematic regimes. In what follows, for definiteness, we focus on the near forward kinematic regime. From now on we omit the labels referring to the particular ($t$- or $u$-) kinematic regime. However, all formulas for the near backward kinematics are essentially the same as in the forward kinematics (after interchanging the momenta). To the leading twist accuracy and to the leading order in the strong coupling $\alpha_s$, the amplitude $\mathcal{M}_\lambda^{s_1 s_2}$ of $\bar{p}p \to \gamma^*\pi^0$ reads

$$\mathcal{M}_\lambda^{s_1 s_2} = \mathcal{C}\frac{1}{(q^2)^2}\Big[\mathcal{S}_\lambda^{s_1 s_2}\mathcal{I}(\xi,t) - \mathcal{S'}_\lambda^{s_1 s_2}\mathcal{I}'(\xi,t)\Big], \tag{3}$$

where

$$\mathcal{C} = -i\frac{(4\pi\alpha_s)^2\sqrt{4\pi\alpha_{em}}f_N^2}{54 f_\pi}\,. \tag{4}$$

Here $\alpha_s$ and $\alpha_{em}$ are the strong and electromagnetic coupling constants, $f_N$ stands for the nucleon wave function normalization constant, and $f_\pi = 93\,\mathrm{MeV}$ denotes the pion weak decay constant. The spin structures in eq. (3) are defined as

$$\begin{aligned}\mathcal{S}_\lambda^{s_1 s_2} &\equiv \bar{V}(p_1, s_1)\hat{\varepsilon}^*(\lambda)\gamma_5 U(p_2, s_2)\\ \mathcal{S'}_\lambda^{s_1 s_2} &\equiv \frac{1}{M}\bar{V}(p_1, s_1)\hat{\varepsilon}^*(\lambda)\hat{\Delta}_T\gamma_5 U(p_2, s_2),\end{aligned} \tag{5}$$

where $V$ and $U$ are the usual nucleon Dirac spinors; $\Delta_T \equiv (k_3 - p_1)_T$ denotes the transverse $t$-channel momentum transfer and the Dirac "hat" notation $\hat{v} = \gamma_\mu v^\mu$ is employed. $\varepsilon(\lambda)$ stands for the polarization vector of the virtual photon. $\mathcal{I}$ and $\mathcal{I}'$ denote the convolution integrals of $\pi N$ TDAs and nucleon DAs with the hard scattering kernels computed from the set of relevant scattering diagrams [4]. The averaged-squared amplitude for the process (1) then reads

$$\begin{aligned}&\overline{|\mathcal{M}^{\bar{p}p\to e^+e^-\pi^0}|^2} =\\ &\frac{1}{4}\sum_{s_1,\,s_2,\,\lambda,\,\lambda'}\mathcal{M}_\lambda^{s_1 s_2}\frac{1}{q^2}e^2\,\mathrm{Tr}\left\{\hat{k}_2\hat{\varepsilon}(\lambda)\hat{k}_1\hat{\varepsilon}^*(\lambda')\right\}\frac{1}{q^2}\left(\mathcal{M}_{\lambda'}^{s_1 s_2}\right)^*.\end{aligned} \tag{6}$$

The differential cross section of the reaction (1) is expressed as

$$\frac{\mathrm{d}\sigma}{\mathrm{d}t\ \mathrm{d}q^2\ \mathrm{d}\cos\theta_\ell^*} = \frac{\int \mathrm{d}\varphi_\ell^*\, |\overline{\mathcal{M}^{\bar{p}p\to e^+e^-\pi^0}}|^2}{64s(s-4M^2)(2\pi)^4}\,, \tag{7}$$

where $\theta_\ell^*$ and $\varphi_\ell^*$ are the lepton polar and azimuthal angles defined in the $e^+e^-$ CM frame (*i.e.* the $\gamma^*$ rest frame).

To the leading twist accuracy, only the transverse polarization states of the virtual photon are contributing. Computing the relevant traces and integrating over the lepton azimuthal angle one gets

$$\begin{aligned}\int \mathrm{d}\varphi_\ell^*\, |\overline{\mathcal{M}^{\bar{p}p\to e^+e^-\pi^0}}|^2\Big|_{\text{Leading twist}} = \\ 2\pi e^2(1+\cos^2\theta_\ell^*)\frac{1}{4}|\mathcal{C}|^2\frac{2(1+\xi)}{\xi(q^2)^4} \\ \times\big(|\mathcal{I}(\xi,t)|^2 - \frac{\Delta_T^2}{M^2}|\mathcal{I}'(\xi,t)|^2\big).\end{aligned} \tag{8}$$

Neglecting $t$ and the nucleon mass squared $M^2$ with respect to large invariants $s$ and $q^2$ (that is a reasonable approximation in the kinematic domain in which the factorized description is assumed to hold) the skewness parameter can be expressed as

$$\xi \simeq \frac{q^2}{2s-q^2}\,. \tag{9}$$

Thus, we work out the following expression for the differential cross section of the reaction (1) within the factorized description in terms of $\pi N$ TDAs in the near-forward kinematic regime:

$$\begin{aligned}\frac{\mathrm{d}\sigma}{\mathrm{d}t\ \mathrm{d}q^2\ \mathrm{d}\cos\theta_\ell^*}\Big|_{\text{Leading twist}} = \\ \frac{K}{s-4M^2}\frac{1}{(q^2)^5}(1+\cos^2\theta_\ell^*),\end{aligned} \tag{10}$$

where

$$\begin{aligned}K = \frac{(4\pi\alpha_{em})^2(4\pi\alpha_s)^4 f_N^4}{64\cdot 54^2(2\pi)^3 f_\pi^2} \\ \times\big(|\mathcal{I}(\xi,t)|^2 - \frac{\Delta_T^2}{M^2}|\mathcal{I}'(\xi,t)|^2\big).\end{aligned} \tag{11}$$

To compute the integral convolution $\mathcal{I}$, $\mathcal{I}'$ we use the revised version of the phenomenological model for $\pi N$ TDAs suggested in refs. [13,28]. Within this approach $\pi N$ TDAs are constrained from the chiral dynamics and expressed through the nucleon DAs relying on the soft pion theorem. Certainly, this is an oversimplified $\pi N$ TDA model that gives non-zero contribution only into the convolution $\mathcal{I}$. Moreover, within this model $\mathcal{I}$ turns to be $\xi$- and $t$-independent. Nevertheless, this model is supposed to provide a reasonable estimate of the normalization for $\pi N$ TDAs and can be taken as reliable at least for sufficiently small transverse momentum transfer. We refer the reader to ref. [29] for the discussion on various phenomenological solutions for the nucleon DA and the relevant values of the strong coupling and nucleon wave function normalization constant. In the present analysis we use the Chernyak-Ogloblin-Zhitnitsky (COZ) [30] phenomenological solution for the nucleon DAs. This solution yields the value $|\mathcal{I}|^2 = 1.69\cdot 10^9$, which is used in our evaluation. For the numerical estimates we use, following ref. [14], the mean value of the strong coupling $\alpha_s = 0.3$ and $f_N = 5.2\cdot 10^{-3}\,\mathrm{GeV}^2$. The cross section (10) serves as the input for the event generator of the signal events $\bar{p}p\to e^+e^-\pi^0$ whose source code [31] was interfaced to the EvtGen [32] Monte Carlo. We remark that the cross section (10) does not contain QED radiative corrections, so the PHOTOS package [33] has been consistently switched off in the GEANT simulation.

For the cross section of the most severe background channel, *i.e.* three-pion production $\bar{p}p\to\pi^+\pi^-\pi^0$, no theoretical calculations in the kinematic region of interest are available and the few existing low-precision measurements [34–38] are not sufficient to constrain models. Inspired by the expectation for the total cross section ratio $\sigma(\bar{p}p\to\pi^+\pi^-)/\sigma(\bar{p}p\to e^+e^-)\sim 10^6$ (see [9,39] and references therein), we have assumed that the same relation holds for the case $\sigma(\bar{p}p\to\pi^+\pi^-\pi^0)/\sigma(\bar{p}p\to e^+e^-\pi^0)$. Even when data sets suggest that three-pion production is about an order of magnitude higher than two-pion production, the totally unknown $\bar{p}p\to e^+e^-\pi^0$ cross section supports the assumption on the signal to background ratio. We remark that in this analysis we reach a very small background pollution on the signal sample. The precise value of the ratio $\sigma(\bar{p}p\to\pi^+\pi^-)/\sigma(\bar{p}p\to e^+e^-)$ is not critical for the conclusions. When the PANDA experiment is running, the measurement of the $\pi^+\pi^-\pi^0$ cross section will be done with great precision, and simultaneously to that of the $e^+e^-\pi^0$ events, so the three-pion cross section will be available to perform background subtraction precisely. In addition, we have assumed that the angular distributions for the three-pion final state $\pi^+\pi^-\pi^0$ are identical to that of the signal final state $e^+e^-\pi^0$. With these considerations in mind, in the event generator for signal events, lepton masses and Monte Carlo identifiers were replaced by the ones correponding to pions to account for background production. This conservative approach represents, from the experimental point of view, the most unfavored situation for background rejection. Having identical distributions for signal and background then requires to rely entirely on particle identification for the discrimination of signal and background events.

Only $\bar{p}p\to\pi^+\pi^-\pi^0$ background events have been simulated in this analysis. As already stated, three-pion production, having the same number of final state particles as that of the signal channel, the same charge signature and together with the small mass gap between electron an pion, constitutes the most severe channel in terms of suppression. Moreover, the assumption of identical angular distributions for signal and background events becomes the worst possible scenario as rejection concerns. In the spirit of a first feasibility study, other possible sources of background are left for future investigations, since their

contribution to the signal pollution is estimated to be minor in comparison with three-pion production. Simple cross section estimations have been done with the help of the Dual Parton Model (DPM) Monte Carlo [40] for some additional background channels. For a compilation of the existing data sets on $\bar{p}$ reactions, see, for instance, ref. [41]. The production cross section for $\bar{p}p \to K^+K^-\pi^0$ is roughly two orders of magnitude smaller than the cross section for the simulated channel $\bar{p}p \to \pi^+\pi^-\pi^0$ over an extended range of $\bar{p}p$ center-of-mass energies. In addition, kaons are much better separable from electrons than pions due to the larger mass gap by means of kinematical fits. The cross section for $\bar{p}p \to \pi^0\pi^0$ is roughly 30 times smaller than that of $\bar{p}p \to \pi^+\pi^-\pi^0$. In $\bar{p}p \to \pi^0\pi^0$, one of the two pions can undergo a Dalitz decay $\pi^0 \to e^+e^-\gamma$, which could fake a signal signature. The Dalitz decay has a branching ratio of 1.2% [42], and thus is suppressed by a factor 2500 compared to $\pi^+\pi^-\pi^0$. Moreover, it has an additional photon. These background events can not be separated from signal events by means of PID only, and additional kinematic cuts will have to be developed if further suppression is needed. Studies of the non-resonant background are beyond the scope of the present analysis. These include exclusive QED channels, like $\bar{p}p \to e^+e^-\gamma\gamma$, as well as photons from uncorrelated events in coincidence with $\bar{p}p \to e^+e^-$ within the data acquisition window. For the latter, dedicated full simulations are needed to make reliable estimates.

One of the key problems we need to address is the experimental verification of the validity of the pQCD-factorization assumption for the reaction in question. Providing evidence of the applicability of the factorized description at relatively low values of $q^2$ represents the most important potential physical result of the suggested measurements. From the theory side (see *e.g.* ref. [43]) several essential marking signs exist for the onset of the collinear factorization regime for hard exclusive reactions:

- Dominance of the specific polarization of the virtual photon.
- Characteristic scaling behaviour of the cross section in $1/q^2$.
- Universality of the corresponding non-perturbative quantities, which means that the same non-perturbative objects provide a satisfactory description to several hard exclusive reactions.

For the case of the nucleon-antinucleon annihilation into a lepton pair in association with a forward (or backward) neutral pion it is the transverse polarization of the virtual photon that is dominant within the collinear factorized description in terms of $\pi N$ TDAs. This dominating contribution manifests itself through the characteristic $(1 + \cos^2\theta^*_\ell)$ behaviour of the cross section (c.f. eq. (10)). This term can be extracted from the experimentally measured cross section through the harmonic analysis in the lepton pair CM scattering angle $\theta^*_\ell$. The characteristic $q^2$-scaling behaviour of the cross section is explicit from eq. (10).

It is worth mentioning that probing experimentally the validity of the collinear factorization assumption for hard exclusive reactions usually represents a challenging task. The test of the scaling behaviour with the available small lever arm in $q^2$ (that is typical for the fixed-target kinematics experiments) turns out to be intricate due to the uncontrollable higher-twist contributions and model dependent implementation of skewness dependence within a particular model for the relevant non-perturbative objects (GPDs or TDAs). Testing factorization will then demand the use of NLO QCD fits to the $q^2$-dependence of the cross section to separate the contributions of the longitudinal and transverse photon polarizations. In a similar way, detailed harmonic analysis will be needed to discriminate between different Fourier components of the $\cos\theta^*_\ell$ distributions. To illustrate these difficulties consider the controversial issue of the applicability of the GPD-formalism-based description of near-forward hard exclusive pion electroproduction off protons. Existing data are suggestive, but not conclusive and the consistency of factorized description still remains to be shown within the experimentally accessible kinematic regime. The $q^2$ dependence of the longitudinal cross section of charged pion electroproduction at JLab Hall C [44] seems to be consistent with the predictions of the leading-twist collinear factorized description already at rather low values of the photon virtuality. However, the transverse cross section is large and its kinematic dependence differs considerably from the scaling expectation. The more recent neutral pion electroproduction data from JLab Hall A and Hall B [45,46] also suggest a large contribution of transversely polarized photons to the cross section, different from the leading-twist formalism that predicts dominance of the longitudinal cross section. Bringing evidence for the validity of QCD factorization for $p\bar{p}$ annihilation into $e^+e^-\pi^0$ in terms of $\pi N$ TDAs will suffer from the same difficulties as the above-mentioned analysis of hard electroproduction of pions at JLab.

Assuming the validity of the leading order factorized description for the signal reaction and adopting a particular normalization for $\pi N$ TDAs, we show the feasibility of measuring of $p\bar{p} \to e^+e^-\pi^0$ with the $\bar{\mathrm{P}}$ANDA detector in the kinematic region where factorization is expected to hold. With the cross section obtained from the simulations we perform simple tests of pQCD at the leading twist, ignoring any higher-order effect. This includes the measurement of the scaling laws by fitting the $q^2$ differential cross sections and the determination of angular distributions by fitting the $\cos\theta^*_\ell$ cross sections.

## 5 Event selection

Several simulations at the center-of-mass energy squared $s = 5\,\mathrm{GeV}^2$ and $s = 10\,\mathrm{GeV}^2$ were done using both simulated signal and background samples in order to determine signal reconstruction efficiency, background rejection power and feasibility of measuring the differential cross section for $\bar{p}p \to e^+e^-\pi^0$ with an integrated luminosity of $2\,\mathrm{fb}^{-1}$.

The analysis procedure for the reconstruction of signal events was designed by tuning the selection cuts in a way that the signal-to-background ratio was kept to its

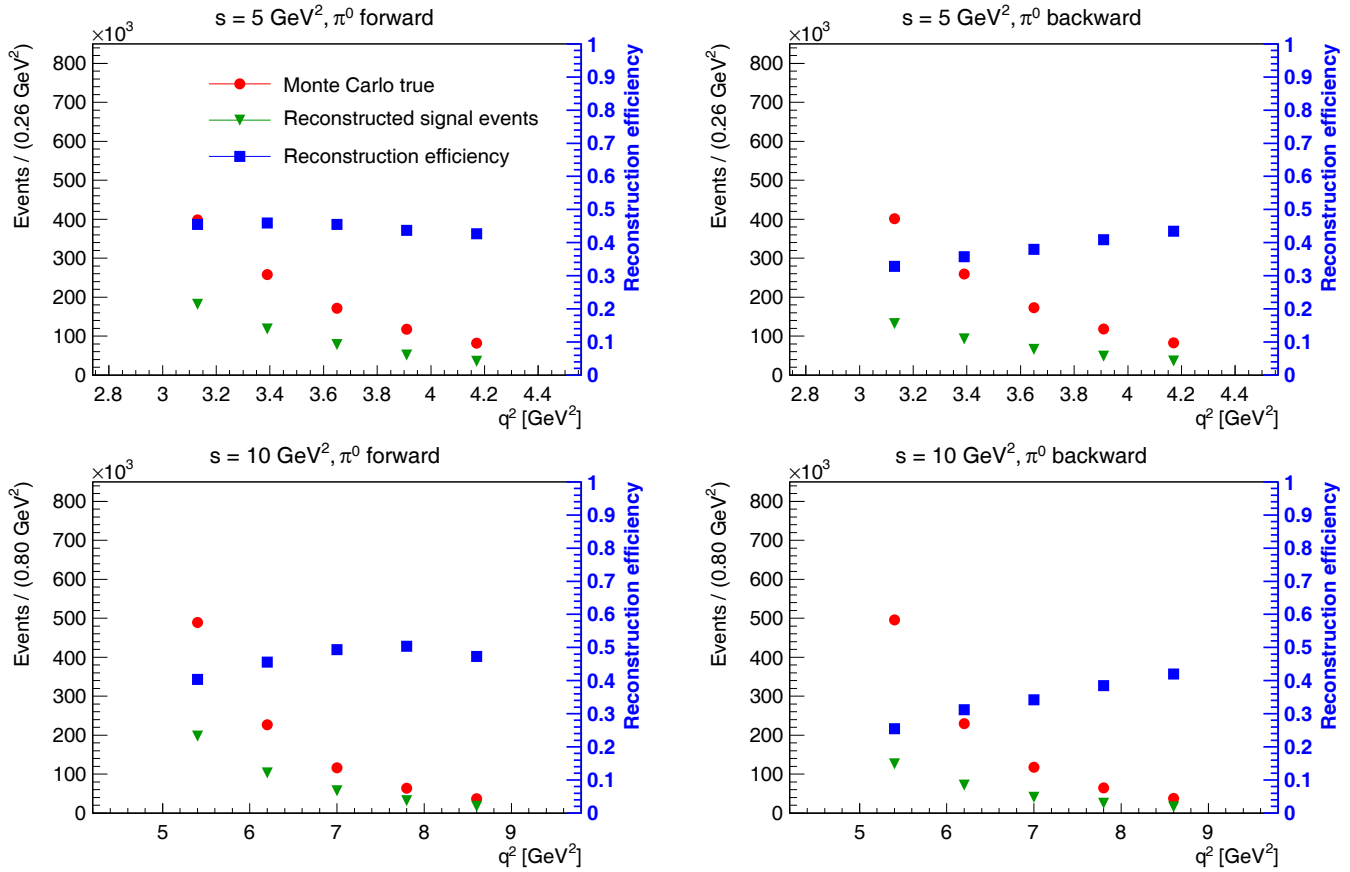


**Fig. 3.** Monte Carlo true $q^2$ distribution for signal events (red dots), reconstructed signal events after event selection (green triangles) and signal reconstruction efficiency (blue squares) as a function of $q^2$ for $s = 5\,\mathrm{GeV}^2$ and $s = 10\,\mathrm{GeV}^2$, in both the $t$- ($\pi^0$ forward) and the $u$- ($\pi^0$ backward) channel kinematic regimes determined using independent statistical samples of $10^6$ generated events.

maximum value in the kinematic region of the measurement. The selection strategy is mainly based on PID cuts. In addition, kinematic fits were used to improve the measurement of the reconstructed momentum and energy of the particles. The reconstruction of $e^+e^-\pi^0$ candidates was done according to the following criteria:

- the event contains exactly two charged tracks of opposite sign;
- the particle associated to the negative track is identified by the PID software as an electron with minimum combined probability of 99% and, at least, with a minimum probability of 10% from each subdetector in $\bar{\mathrm{P}}$ANDA;
- the particle associated to the positive track is identified by the PID software as a positron with minimum combined probability of 99% and, at least, with a minimum probability of 10% from each subdetector in $\bar{\mathrm{P}}$ANDA;
- in the event, two photon candidates are reconstructed from two energy deposits in the EMC with a photon energy threshold $E_\gamma > 0.03\,\mathrm{GeV}$ and no track associated, and combined to give a $\pi^0$ candidate with an invariant mass $0.115 < M(\gamma,\gamma) < 0.150\,\mathrm{GeV}$.

At $s = 5\,\mathrm{GeV}^2$ and $s = 10\,\mathrm{GeV}^2$, signal events were measured in the kinematic range $3.0 < q^2 < 4.3\,\mathrm{GeV}^2$ and $5 < q^2 < 9\,\mathrm{GeV}^2$, respectively. In both cases, a $\pi^0$ candidate was reconstructed in the forward or backward region $|\cos\theta_{\pi^0}| > 0.5$, where the polar angle of the neutral pion is measured with respect to the direction of the antiproton in the $\bar{p}p$ CM system. The kinematic region of the measurement ensures that, at each $(q^2, \cos\theta_{\pi^0})$ point of the phase space, the appropiate momentum transfer squared ($t$ or $u$ for the forward and backward pion production, respectively) remains below 10% of the $q^2$ value. This is the definition adopted in this analysis of $|t| \ll q^2$ and $|u| \ll q^2$, needed to preserve the applicability of the QCD collinear factorization description.

## 6 Signal reconstruction efficiency

High statistics simulations were done for the signal channel $\bar{p}p \to e^+e^-\pi^0$ in order to determine the efficiency factors needed to correct raw data for detector effects, including efficiency in the reconstruction and bin migrations. On the basis of a full Monte Carlo simulation, the reconstruction efficiency measured in a given bin of a

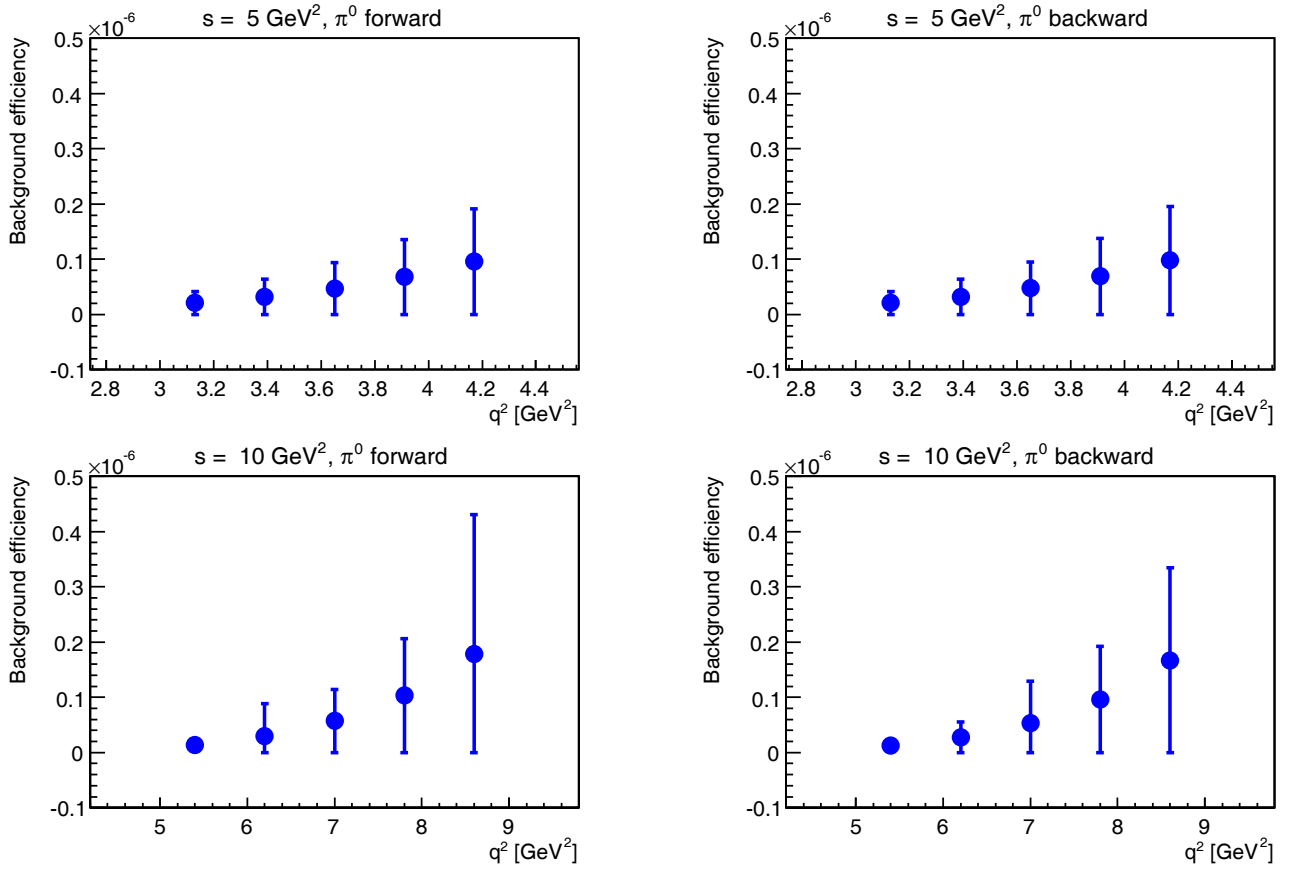


**Fig. 4.** Upper limit for the background reconstruction efficiency at the confidence level of 67.3% as a function of $q^2$ for $s = 5\,\mathrm{GeV}^2$ and $s = 10\,\mathrm{GeV}^2$, in both the $t$- ($\pi^0$ forward) and the $u$- ($\pi^0$ backward) channel kinematic regimes determined using independent statistical samples of $10^8$ generated events.

generic observable $X$ is commonly defined as $\epsilon = N^R/N^G$, where $N^R$ and $N^G$ are the number of reconstructed and generated events found in that bin, with standard deviation $\Delta\epsilon = \sqrt{N^R}/N^G$ assuming a Poisson distribution. In order to determine the signal reconstruction efficiencies as a function of $q^2$, two full Monte Carlo simulations using $10^6$ generated events each were performed at the center-of-mass energy squared $s = 5\,\mathrm{GeV}^2$ in the $q^2$ range $3.0 < q^2 < 4.3\,\mathrm{GeV}^2$, one in the $t$-channel regime, with the neutral pion in the forward region, and another one in the $u$-channel regime, with the neutral pion in the backward region. In an analogous way, two additional full simulations with the same statistics were performed at $s = 10\,\mathrm{GeV}^2$, in the range $5 < q^2 < 9\,\mathrm{GeV}^2$ also for both the $t$- and the $u$-channel regimes. The obtained reconstruction efficiencies in bins of $q^2$ are shown in fig. 3 for all four cases. At $s = 5\,\mathrm{GeV}^2$ the reconstruction efficiency shows a stable behaviour in $q^2$, with an almost constant value around 45% in the $t$-channel regime, whereas in the $u$-channel regime the efficiency exhibits an increasing pattern from 33% to 43% in the $q^2$ range. At $s = 10\,\mathrm{GeV}^2$ a similar behaviour is observed, with a mean value of 45% in the $t$-channel regime and increasing the reconstruction efficiency from 25% to 40% with $q^2$ in the $u$-channel regime.

## 7 Background suppression

Analogous simulations to the ones described in sect. 6 were performed using samples of $10^8$ $\bar{p}p \to \pi^+\pi^-\pi^0$ generated events in order to measure the background suppression power achieved by the selection criteria defined in sect. 5. At $s = 5\,\mathrm{GeV}^2$ and for both the $t$- and the $u$-channel regimes, no pions were found after event selection. At $s = 10\,\mathrm{GeV}^2$, four $\pi^+\pi^-\pi^0$ events were misidentified as $e^+e^-\pi^0$ events in the $t$-channel regime, whereas in the $u$-channel regime only one background event survived the cuts. The background suppression factor is defined as the inverse of the probability that a $\pi^+\pi^-\pi^0$ event is misidentified as a $e^+e^-\pi^0$ event. This probability can in fact be measured as the "efficiency" in the reconstruction of background events when a $\pi^+\pi^-\pi^0$ sample is filtered by an algorithm designed to reconstruct $e^+e^-\pi^0$ events. For this reason, we denote this probability as $\epsilon_B$. In situations of high suppression like this one, where only a few (or even no event) are (is) reconstructed in a given bin, the standard estimation of efficiency and its error based on binomial or Poisson distributions gives results in contradiction with intuition. For instance, if no pion event is reconstructed in a given bin, the value for the efficiency would be zero with complete certainty (zero error) accord-

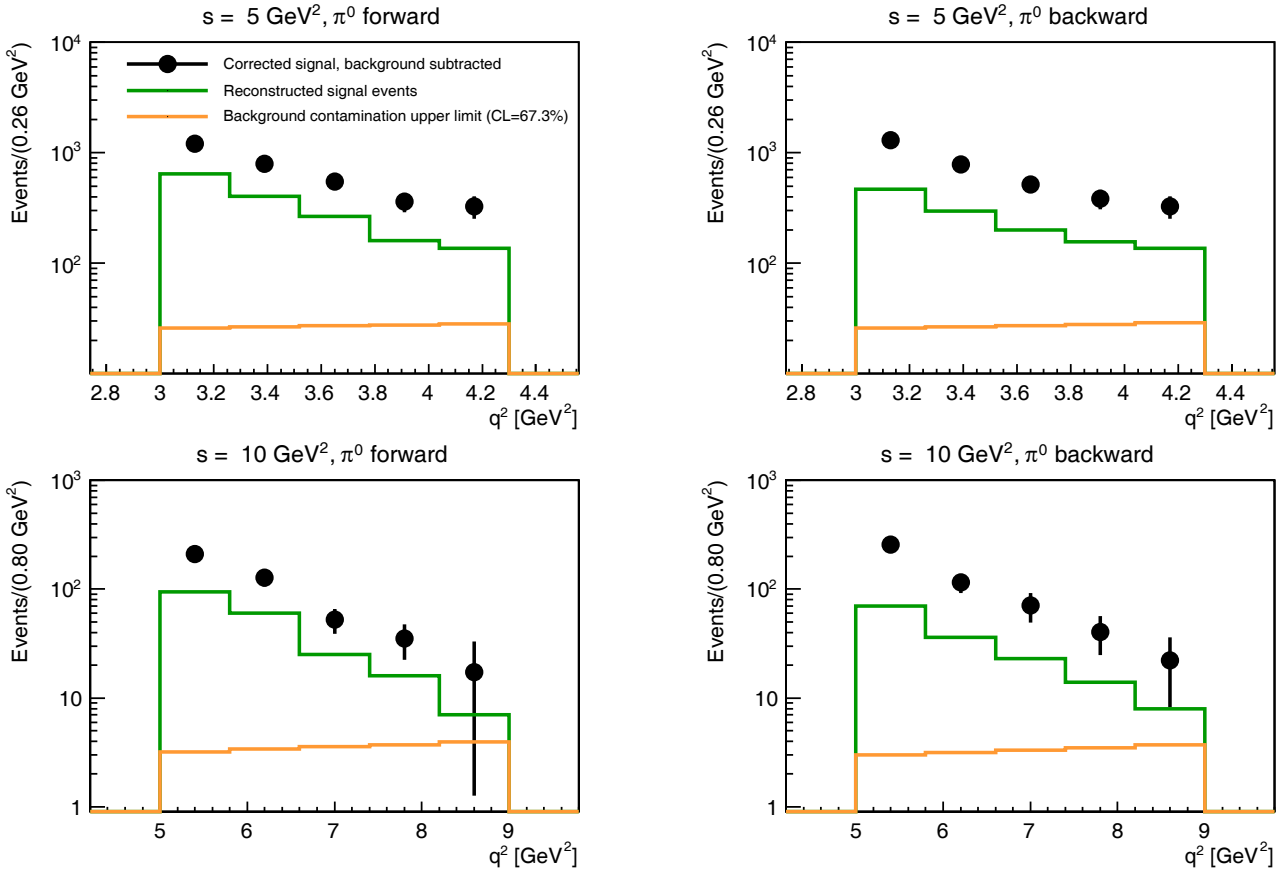


**Fig. 5.** The reconstructed signal after event selection (green), the expected upper limit background contamination at the 67.3% of confidence level (orange) and the reconstructed, efficiency-corrected signal after background subtraction (black) in bins of $q^2$, for $s = 5\,\mathrm{GeV}^2$ and $s = 10\,\mathrm{GeV}^2$ in both the $t$- ($\pi^0$ forward) and the $u$- ($\pi^0$ backward) channel kinematic regimes using statistical samples of integrated luminosity $\mathcal{L} = 2\,\mathrm{fb}^{-1}$.

ing to the Poisson distribution. We can still in this case estimate an *upper limit* for $\epsilon_B$ at some value of confidence level, depending on the available statistics. In this analysis, to measure the reconstruction efficiency and its error, a Bayesian approach which exhibits reasonable behaviour in the limit of high suppression has been used to treat the background channel (see ref. [47] for a review). At the 67.3% of confidence level (*i.e.* one sigma) estimators of the upper limit of $\epsilon_B$ and its standard deviation $\Delta\epsilon_B$ are given by the relations [47]:

$$\epsilon_B = \frac{N^R + 1}{N^G + 2}$$
$$\Delta\epsilon_B = \sqrt{\left(\frac{N^R + 1}{N^G + 2}\right)\left\{\frac{N^R + 2}{N^G + 3} - \frac{N^R + 1}{N^G + 2}\right\}}. \qquad (12)$$

For the two energies simulated and in both, the $t$- and the $u$-channel regimes, misidentification probabilities in bins of $q^2$ have been estimated in this way and are displayed in fig. 4. The inverse $1/\epsilon_B$ then yields the suppression factor. At $s = 5\,\mathrm{GeV}^2$, the simulations show that the background suppression factor goes from $5{\cdot}10^7$ at low $q^2$ down to $1{\cdot}10^7$ at large $q^2$. At $s = 10\,\mathrm{GeV}^2$, the background suppression factor goes from $1 \cdot 10^8$ at low $q^2$ down to $6 \cdot 10^6$ at large $q^2$. Under the assumption of a background to signal cross section ratio $\sigma(\bar{p}p \to \pi^+\pi^-\pi^0)/\sigma(\bar{p}p \to e^+e^-\pi^0) = 10^6$, this means that the background pollution in a signal sample will remain at the level of a few percent after event selection for low $q^2$, whereas at larger values of $q^2$ it can be kept below 20%. In case the cross section ratio is much larger than $10^6$, a better background suppression can be achieved at the cost of reducing the signal efficiency. The estimated upper limit of background pollution in a signal sample, necessary for the subsequent statistical subtraction, is discussed in detail in appendix B.

## 8 Feasibility of measuring the $\bar{p}p \to e^+e^-\pi^0$ differential cross section using an integrated luminosity $\mathcal{L} = 2\,\mathrm{fb}^{-1}$

The feasibility of measuring the production cross section for the signal channel $\bar{p}p \to e^+e^-\pi^0$ requires simulations using the expected statistics corresponding to some particular value of integrated luminosity. Running periods of six months with the average design luminosity of $1.5 \cdot 10^{32}\,\mathrm{cm}^{-2}\,\mathrm{s}^{-1}$ will provide $2\,\mathrm{fb}^{-1}$ of integrated

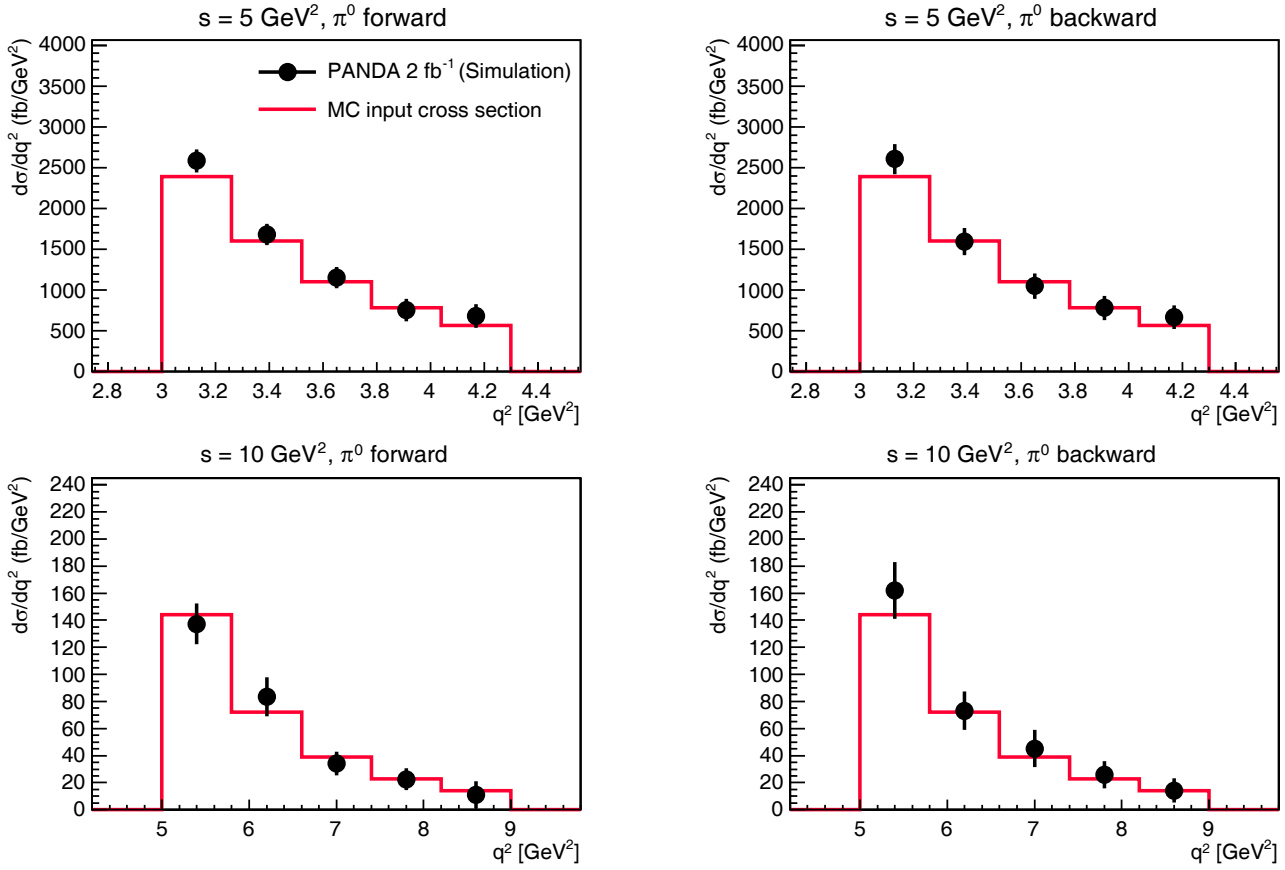


**Fig. 6.** The (background subtracted) $\bar{p}p \to e^+e^-\pi^0$ differential cross section from the simulation $(\mathrm{d}\sigma/\mathrm{d}q^2)_{\mathrm{sim}}$ in bins of $q^2$ with a statistical sample of integrated luminosity $\mathcal{L} = 2\,\mathrm{fb}^{-1}$, compared to the theoretical input in the Monte Carlo, for $s = 5\,\mathrm{GeV}^2$ and $s = 10\,\mathrm{GeV}^2$, in both the $t$- ($\pi^0$ forward) and the $u$- ($\pi^0$ backward) channel kinematic regimes.

luminosity in $\bar{\mathrm{P}}$ANDA [7]. In order to estimate the corresponding statistics, we have first extrapolated the differential cross section given by eq. (10), which corresponds to the limit of neutral pion with zero transverse momentum, into the forward and backward cone $|\cos\theta_{\pi_0}| > 0.5$. Second, the extrapolated differential cross section was integrated in the kinematic region of the measurement. At $s = 5\,\mathrm{GeV}^2$, integration in the range $3.0 < q^2 < 4.3\,\mathrm{GeV}^2$ and $|\cos\theta_{\pi_0}| > 0.5$ gave a value of 1675 fb for the integrated cross section. At $s = 10\,\mathrm{GeV}^2$, integration in the range $5 < q^2 < 9\,\mathrm{GeV}^2$ and $|\cos\theta_{\pi_0}| > 0.5$ gave a value of 233 fb for the integrated cross section. Details on the extrapolation and integration of the differential cross section in a two-dimensional bin $(\Delta q^2, \Delta\cos\theta_{\pi_0})$ can be found in appendix A. The expected number of signal events in $\bar{\mathrm{P}}$ANDA using $\mathcal{L} = 2\,\mathrm{fb}^{-1}$ are then 3350 and 465 at $s = 5\,\mathrm{GeV}^2$ and $s = 10\,\mathrm{GeV}^2$, respectively, both in the $t$- and the $u$-channel kinematic regimes. For each value of $s$, two full simulations have been performed using these statistical samples in both channels. Then, the raw reconstructed distributions have been corrected bin by bin in $q^2$ with the efficiency factors $\epsilon$ determined by the high statistics simulations described in sect. 6. In addition, in each of the simulations and for each $q^2$ bin, the remaining background contamination which would survive the selection of signal events in a data sample of $2\,\mathrm{fb}^{-1}$ has been estimated. The estimation was done on the basis of the background efficiency factors discussed in sect. 7 (eq. (12)) and assuming a ratio $\sigma(\bar{p}p \to \pi^+\pi^-\pi^0)/\sigma(\bar{p}p \to e^+e^-\pi^0) = 10^6$. Consequently, the statistical error in the number of reconstructed signal events $N^R$ has been corrected to take into account the subtraction of the estimated upper limit background contamination. Details on the background subtraction procedure are given in appendix B. An upper limit of background pollution at the level of a few percent is expected at low $q^2$, remaining below 20% at large values of $q^2$. The raw reconstructed signal after event selection, the expected upper limit background contamination, and the efficiency-corrected signal after background subtraction are shown in fig. 5 for the two energies simulated, in both the $t$- and the $u$-channel regimes. The differential cross section obtained from the simulation in a $q^2$ bin with width $\Delta q^2$ (integrated over $\cos\theta_{\pi^0} > 0.5$ in the $t$-channel regime and over $\cos\theta_{\pi^0} < -0.5$ in the $u$-channel regime) is then determined as

$$\left(\frac{\mathrm{d}\sigma}{\mathrm{d}q^2}\right)_{\mathrm{sim}} = \frac{N^R}{\epsilon \cdot \mathcal{L} \cdot \Delta q^2}\,. \tag{13}$$

The differential cross section obtained from the simulations $(\mathrm{d}\sigma/\mathrm{d}q^2)_{\mathrm{sim}}$ in bins of $q^2$ together with the input

**Table 1.** The differential cross section obtained from the simulations $(\mathrm{d}\sigma/\mathrm{d}q^2)_{\mathrm{sim}}$ and its statistical error $\Delta_{\mathrm{stat}}$ in bins of $q^2$, compared to the input cross section in the Monte Carlo $(\mathrm{d}\sigma/\mathrm{d}q^2)_{\mathrm{MC}}$, for $s = 5\,\mathrm{GeV}^2$ in both the $t$- and the $u$-channel kinematic regimes. In each $q^2$ bin, the cross section is integrated in $|\cos\theta_{\pi^0}| > 0.5$.

| $s = 5\,\mathrm{GeV}^2$, $t$-channel ($\pi^0$ forward) | | | |
|---|---|---|---|
| $q^2$ bin ($\mathrm{GeV}^2$) | $(\mathrm{d}\sigma/\mathrm{d}q^2)_{\mathrm{sim}}$ ($\mathrm{fb}/\mathrm{GeV}^2$) | $\Delta_{\mathrm{stat}}$ ($\mathrm{fb}/\mathrm{GeV}^2$) | $(\mathrm{d}\sigma/\mathrm{d}q^2)_{\mathrm{MC}}$ ($\mathrm{fb}/\mathrm{GeV}^2$) |
| 3.00, 3.26 | 2584 | 140 | 2388 |
| 3.26, 3.52 | 1682 | 132 | 1600 |
| 3.52, 3.78 | 1152 | 131 | 1105 |
| 3.78, 4.04 | 754 | 136 | 782 |
| 4.04, 4.30 | 680 | 145 | 567 |

| $s = 5\,\mathrm{GeV}^2$, $u$-channel ($\pi^0$ backward) | | | |
|---|---|---|---|
| $q^2$ bin ($\mathrm{GeV}^2$) | $(\mathrm{d}\sigma/\mathrm{d}q^2)_{\mathrm{sim}}$ ($\mathrm{fb}/\mathrm{GeV}^2$) | $\Delta_{\mathrm{stat}}$ ($\mathrm{fb}/\mathrm{GeV}^2$) | $(\mathrm{d}\sigma/\mathrm{d}q^2)_{\mathrm{MC}}$ ($\mathrm{fb}/\mathrm{GeV}^2$) |
| 3.00, 3.26 | 2605 | 186 | 2388 |
| 3.26, 3.52 | 1591 | 166 | 1600 |
| 3.52, 3.78 | 1048 | 157 | 1105 |
| 3.78, 4.04 | 782 | 150 | 782 |
| 4.04, 4.30 | 667 | 147 | 567 |

**Table 2.** The differential cross section obtained from the simulations $(\mathrm{d}\sigma/\mathrm{d}q^2)_{\mathrm{sim}}$ and its statistical error $\Delta_{\mathrm{stat}}$ in bins of $q^2$, compared to the input cross section in the Monte Carlo $(\mathrm{d}\sigma/\mathrm{d}q^2)_{\mathrm{MC}}$, for $s = 10\,\mathrm{GeV}^2$ in both the $t$- and the $u$-channel kinematic regimes. In each $q^2$ bin, the cross section is integrated in $|\cos\theta_{\pi^0}| > 0.5$.

| $s = 10\,\mathrm{GeV}^2$, $t$-channel ($\pi^0$ forward) | | | |
|---|---|---|---|
| $q^2$ bin ($\mathrm{GeV}^2$) | $(\mathrm{d}\sigma/\mathrm{d}q^2)_{\mathrm{sim}}$ ($\mathrm{fb}/\mathrm{GeV}^2$) | $\Delta_{\mathrm{stat}}$ ($\mathrm{fb}/\mathrm{GeV}^2$) | $(\mathrm{d}\sigma/\mathrm{d}q^2)_{\mathrm{MC}}$ ($\mathrm{fb}/\mathrm{GeV}^2$) |
| 5.0, 5.8 | 137 | 15 | 144 |
| 5.8, 6.6 | 83 | 14 | 72 |
| 6.6, 7.4 | 34 | 9 | 39 |
| 7.4, 8.2 | 23 | 8 | 23 |
| 8.2, 9.0 | 11 | 10 | 14 |

| $s = 10\,\mathrm{GeV}^2$, $u$-channel ($\pi^0$ backward) | | | |
|---|---|---|---|
| $q^2$ bin ($\mathrm{GeV}^2$) | $(\mathrm{d}\sigma/\mathrm{d}q^2)_{\mathrm{sim}}$ ($\mathrm{fb}/\mathrm{GeV}^2$) | $\Delta_{\mathrm{stat}}$ ($\mathrm{fb}/\mathrm{GeV}^2$) | $(\mathrm{d}\sigma/\mathrm{d}q^2)_{\mathrm{MC}}$ ($\mathrm{fb}/\mathrm{GeV}^2$) |
| 5.0, 5.8 | 162 | 21 | 144 |
| 5.8, 6.6 | 73 | 14 | 72 |
| 6.6, 7.4 | 45 | 14 | 39 |
| 7.4, 8.2 | 26 | 10 | 23 |
| 8.2, 9.0 | 14 | 9 | 14 |

cross section in the Monte Carlo $(\mathrm{d}\sigma/\mathrm{d}q^2)_{\mathrm{MC}}$ are shown in tables 1 and 2 and are displayed in fig. 6. For the comparison, the input cross section in the Monte Carlo, which follows a $1/(q^2)^5$ distribution (see eq. (10)), was normalized to the value of the integrated cross section in the kinematic region of the measurement. At $s = 5\,\mathrm{GeV}^2$, the expected precision of the measurement goes from 5% at low $q^2$ to 21% at high $q^2$ in the $t$-channel regime, and from 7% to 22% in the $u$-channel regime. At $s = 10\,\mathrm{GeV}^2$, the statistical error goes from 11% up to 91% in the $t$-channel regime, and from 13% up to 64% in the $u$-channel regime. The results show that the signal channel identification and background separation at $s = 5\,\mathrm{GeV}^2$ is feasible, with averaged statistical precision of 12% (excluding the last $q^2$ bin with poor statistics). At $s = 10\,\mathrm{GeV}^2$, the lower statistics increases the averaged uncertainty to 24%.

Bringing evidence for the consistency of the predictions by leading twist pQCD factorization with the experimentally measured $p\bar{p} \to \ell^+\ell^-\pi^0$ cross section represents the major goal of the proposed experimental studies. The harmonic analysis for separating the contribution of the transversely polarized virtual photon as well as the $1/q^2$-scaling studies are the first crucial tests to be carried out to check the validity of the pQCD factorized description once sufficiently high quality experimental data appear.

In our Monte Carlo studies the scaling exponent is measured by fitting the $q^2$ distributions obtained from the simulations. The fit function results from averaging the theoretical $\mathrm{d}\sigma/\mathrm{d}q^2$ in $q^2$ bins:

$$f(q^2) = \frac{1}{a}\int_{q^2-a/2}^{q^2+a/2} \mathrm{d}x\ B\ \frac{1}{x^A}\,, \qquad (14)$$

which matches the measured observable. Here, the scaling parameter $A$ ($A = 5.0$ is the input to the event generator) and the normalization constant $B$ are the fit parameters and $a$ is the $q^2$ bin width ($a = 0.26\,\mathrm{GeV}^2$ at $s = 5\,\mathrm{GeV}^2$ and $a = 0.80\,\mathrm{GeV}^2$ at $s = 10\,\mathrm{GeV}^2$). The fitted $q^2$ distributions together with the measured values of $A$ and $B$ are displayed in fig. 7 for the two values of energy simulated in both the $t$- and $u$-channel regimes. Using the measured values from all four fits, the scaling exponent $A$ has an average value of 5.2 with a standard deviation of 0.3. The large errors in the normalization constants obtained from the fits are due to the strong correlation between the two fit parameters.

Repeating the same steps which led to the determination of the differential cross sections $\mathrm{d}\sigma/\mathrm{d}q^2$, as described at the beginning of this section, the distributions $\mathrm{d}\sigma/\mathrm{d}\cos\theta^*_\ell$ have been also determined from the simulations. The full kinematic range $-1 < \cos\theta^*_\ell < 1$ is covered with a total of 8 bins for both energies and channels. At the leading twist and as a consequence of the dominance of the transverse polarization of the virtual photon, the cross section in $\cos\theta^*_\ell$ follows a distribution $(1 + \cos^2\theta^*_\ell)$. The cross sections obtained from the simulations were then fitted using the bin average of the theoretical expectation:

$$g(\cos\theta^*_\ell) = \frac{1}{b}\int_{\cos\theta^*_\ell - b/2}^{\cos\theta^*_\ell + b/2} \mathrm{d}x\ D(1 + Cx^2). \qquad (15)$$

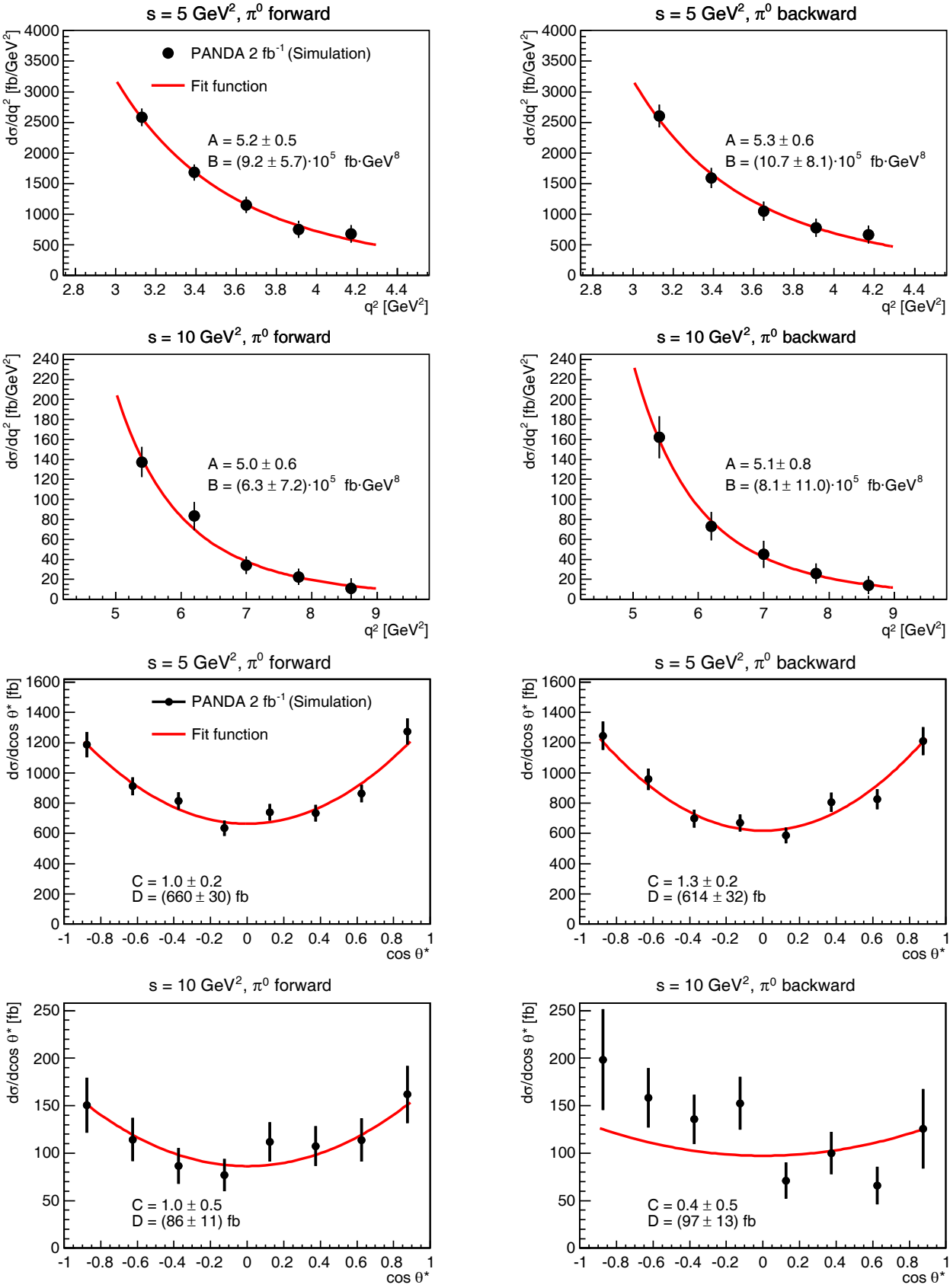


**Fig. 7.** The $\bar{p}p \to e^+e^-\pi^0$ differential cross sections obtained from the simulations (integrated luminosity $\mathcal{L} = 2\,\mathrm{fb}^{-1}$) for $s = 5\,\mathrm{GeV}^2$ and $s = 10\,\mathrm{GeV}^2$, in both the $t$- ($\pi^0$ forward) and the $u$- ($\pi^0$ backward) channel kinematic regimes are fitted with the theoretical leading twist predictions. For both the $q^2$ and $\cos\theta^*_\ell$ distributions, the fit function is integrated over bin width. The average value for the $q^2$ scaling exponent is $A = 5.2 \pm 0.3$. The average value for the $\cos\theta^*_\ell$ prefactor is $C = 0.9 \pm 0.2$.

Here, the prefactor $C$ ($C = 1$ is the input to the event generator) and the normalization constant $D$ are the fit parameters and $b = 0.25$ is the bin width. The fitted $\cos\theta_\ell^*$ distributions together with the measured values of $C$ and $D$ are shown in fig. 7 for the two energies and channels. Using the measured values from all four fits, the prefactor $C$ has an average value of 0.9 with a standard deviation of 0.2. The uncertainty in the prefactor $C$ contains the uncertainty in the reconstructed $q^2$, which is used to boost the $e^+$ and $e^-$ four momenta to the $\gamma^*$ rest frame in order to reconstruct the variable $\cos\theta_\ell^*$. Therefore, one expects to measure the $\cos\theta_\ell^*$ prefactor $C$ with less precision than the $q^2$ scaling exponent $A$.

## 9 Conclusions and outlook

In the framework of the $\bar{\text{P}}$ANDA@FAIR experiment, cross section measurements of nucleon-antinucleon annihilation into a highly virtual lepton pair in association with a pion emitted in the forward or the backward region will represent a novel test of the QCD collinear factorization approach of hard exclusive reactions providing experimental access to the $\pi N$ TDAs.

In this paper we address the feasibility of measuring $\bar{p}p \to e^+e^-\pi^0$ with the $\bar{\text{P}}$ANDA detector for the center-of-mass energy squared $s = 5\,\text{GeV}^2$ and $s = 10\,\text{GeV}^2$ for the kinematic regimes in which the factorized description of the process in terms of $\pi N$ TDAs and proton DAs can be assumed. For $s = 5\,\text{GeV}^2$, the kinematic region of the measurement was $3.0 < q^2 < 4.3\,\text{GeV}^2$, with the neutral pion scattered into the forward (or backward) cone selected by the condition $|\cos\theta_{\pi^0}| > 0.5$. For $s = 10\,\text{GeV}^2$, the kinematic region of the measurement was $5 < q^2 < 9\,\text{GeV}^2$, with $|\cos\theta_{\pi^0}| > 0.5$.

The input cross section for the event generator of signal events is the leading-twist, leading-order calculation which uses $\pi N$ TDAs and nucleon DAs within the collinear factorization approach. In our studies we employed the simple $\pi N$ TDA model constraining $\pi N$ TDAs from chiral dynamics in terms of nucleon DAs. This model is argued to provide a reliable normalization for $\pi N$ TDAs for the pion being produced exactly in the forward (backward) direction. Therefore, this model at least represents a reasonable first step approximation. Future detailed feasibility studies will require the use of a more sophisticated phenomenological model proposed for $\pi N$ TDAs in [5] based on the spectral representation for baryon-to-meson TDAs in terms of quadruple distributions [48]. Another possibility is given by the calculations of $\pi N$ TDAs within the light-cone quark model approach [49].

Our simulations at $s = 5\,\text{GeV}^2$ show that $\bar{\text{P}}$ANDA particle identification capabilities will allow a suppression of the hadronic background $\bar{p}p \to \pi^+\pi^-\pi^0$ at the level of $5 \cdot 10^7$ at low $q^2$, decreasing to $1 \cdot 10^7$ for the larger values of $q^2$. At $s = 10\,\text{GeV}^2$, the suppression factor remains around $1 \cdot 10^8$ at low $q^2$, down to $6 \cdot 10^6$ for large $q^2$. For both energies, the signal reconstruction efficiency is kept at about 40% on average. Consequently, we expect that the pion pollution in the signal sample will remain at the level of a few percent at low $q^2$, and under control below 20% for larger values of four-momentum transfer squared. The dedicated studies were performed with the statistics expected for an integrated luminosity of $2\,\text{fb}^{-1}$ and show that the future measurement of the differential production cross section in bins of $q^2$ is feasible with $\bar{\text{P}}$ANDA, with averaged statistical uncertainty of 12% at $s = 5\,\text{GeV}^2$, and with averaged statistical uncertainty of 24% at $s = 10\,\text{GeV}^2$. The cross sections obtained from the simulations in $q^2$ and $\cos\theta_\ell^*$ were also fitted to test pQCD factorization at the lowest order. According to the simulations, the measured value for the $q^2$ scaling exponent is $A = 5.2 \pm 0.3$. In the lepton angular distributions, the measured value for the $\cos\theta_\ell^*$ prefactor is $C = 0.9 \pm 0.2$. These results are promising concerning the experimental perspectives for addressing the issue of validity of the pQCD factorized description of the $\bar{p}p \to \ell^+\ell^-\pi^0$ reaction in terms of $\pi N$ TDAs and accessing $\pi N$ TDAs with $\bar{\text{P}}$ANDA. Other kinematic regions and other processes [16, 50] related to TDAs should be scrutinized in a similar way to evaluate their feasibility.

The success of this work relies critically on the expertise and dedication of the computing organizations that support $\bar{\text{P}}$ANDA. We acknowledge financial support from the Science and Technology Facilities Council (STFC), British funding agency, Great Britain; the Bhabha Atomic Research Center (BARC) and the Indian Institute of Technology, Mumbai, India; the Bundesministerium für Bildung und Forschung (BMBF), Germany; the Carl-Zeiss-Stiftung 21-0563-2.8/122/1 and 21-0563-2.8/131/1, Mainz, Germany; the Center for Advanced Radiation Technology (KVI-CART), Groningen, Netherlands; the CNRS/IN2P3, France; the Deutsche Forschungsgemeinschaft (DFG), Germany; the Deutscher Akademischer Austauschdienst (DAAD), Germany; the Forschungszentrum Jülich GmbH, Jülich, Germany; the FP7 GA283286, European Commission funding; the Gesellschaft für Schwerionenforschung GmbH (GSI), Darmstadt, Germany; the Helmholtz-Gemeinschaft Deutscher Forschungszentren (HGF), Germany; the INTAS, European Commission funding; the Institute of High Energy Physics (IHEP) and the Chinese Academy of Sciences, Beijing, China; the Istituto Nazionale di Fisica Nucleare (INFN), Italy; the Ministerio de Educación y Ciencia (MEC) FPA2006-12120-C03-02, the Instituto de Fisica Corpuscular (IFIC) and the Universidad de Valencia-CSIC, Paterna, Spain; the National Science Center of Poland (NCN) and the Polish Ministry of Science and Higher Education (MNiSW), Poland; the State Atomic Energy Corporation Rosatom and National Research Center "Kurchatov Institute", Russia; the Schweizerischer Nationalfonds zur Forderung der wissenschaftlichen Forschung (SNF), Switzerland; the Stefan Meyer Institut für Subatomare Physik and the Österreichische Akademie der Wissenschaften, Wien, Austria; the Swedish Research Council, Sweden. We would like to thank B. Pire, L. Szymanowski and J.P. Lansberg for constructive and stimulating discussions, lots of explanations on the topic of the TDAs and for a careful reading of the manuscript. Finally, we are very grateful to D. Djukanovic for his invaluable work in maintaining the dedicated HIMSTER cluster at Helmholtz-Institut Mainz, where the simulations of this paper have been performed.

**Open Access** This is an open access article distributed under the terms of the Creative Commons Attribution License (http://creativecommons.org/licenses/by/4.0), which permits unrestricted use, distribution, and reproduction in any medium, provided the original work is properly cited.

## Appendix A. Integration in a $(\Delta q^2, \Delta \cos\theta_{\pi^0})$ bin

In this appendix we describe the extrapolation and integration of the differential cross section (10) in the kinematic region of the measurement defined by the two-dimensional bin $(\Delta q^2, \Delta \cos\theta_{\pi^0})$.

The kinematics of $\bar{p}(p_1)p(p_2) \to \gamma^*(q)\pi^0(k_3)$ is most easily solved in the CM frame, where the total three-momentum of both the initial and final state is zero. By convention, the direction of the antiproton defines the positive $z$-direction of the coordinate system. Also by convention, the $x$-axis of the coordinate system is chosen to be perpendicular to the scattering plane. With this choice, the four-momenta of the initial- and final-state particles become

$$\begin{aligned} p_1 &= (E, 0, 0, k_i) \\ p_2 &= (E, 0, 0, -k_i) \\ q &= (E_\gamma, 0, -k_f \sin\theta_{\pi^0}, -k_f \cos\theta_{\pi^0}) \\ k_3 &= (E_{\pi^0}, 0, k_f \sin\theta_{\pi^0}, k_f \cos\theta_{\pi^0}), \end{aligned} \tag{A.1}$$

with energies given by $E = \sqrt{M^2 + k_i^2}$, $E_\gamma = \sqrt{q^2 + k_f^2}$ and $E_{\pi^0} = \sqrt{m_{\pi^0}^2 + k_f^2}$. The condition $2E = \sqrt{s}$ fixes the three-momentum modulus squared of both proton and antiproton to be

$$k_i^2 = \frac{1}{4}(s - 4M^2). \tag{A.2}$$

In the same way, the energy conservation relation in the final state $E_\gamma + E_{\pi^0} = \sqrt{s}$ fixes the momenta of virtual photon and neutral pion, with the result

$$k_f^2 = \frac{1}{4s}\left[s^2 - 2(q^2 + m_{\pi^0}^2)s + (q^2 - m_{\pi^0}^2)^2\right]. \tag{A.3}$$

Using the four-momenta given by eq. (A.1), the antiproton to pion four-momentum transfer squared $t \equiv (p_1 - k_3)^2$ is given by

$$\begin{aligned} t &= (p_1 - k_3)^2 \\ &= p_1^2 + k_3^2 - 2p_1 \cdot k_3 \\ &= M^2 + m_{\pi^0}^2 - 2(EE_{\pi^0} - k_i k_f \cos\theta_{\pi^0}), \end{aligned} \tag{A.4}$$

which can be written as

$$\begin{aligned} t = \frac{1}{2}\big[&m_{\pi^0}^2 + \cos\theta_{\pi^0}\sqrt{1 - 4M^2/s}\ \Lambda(s, q^2, m_{\pi^0}^2) \\ &+ 2M^2 + q^2 - s\big], \end{aligned} \tag{A.5}$$

with $\Lambda(x, y, z) \equiv \sqrt{x^2 + y^2 + z^2 - 2xy - 2xz - 2yz}$. Equation (A.5) expresses the dependence of the variable $t$ on $q^2$ and $\cos\theta_{\pi^0}$ for a given value of the center-of-mass energy squared $s$.

The integration of the leptonic phase space degrees of freedom in eq. (10) is straightforward:

$$\begin{aligned} \frac{\mathrm{d}\sigma}{\mathrm{d}t\ \mathrm{d}q^2}\bigg|_{\Delta_T=0} &= \int_{-1}^{1} \mathrm{d}\cos\theta_\ell^* \frac{\mathrm{d}\sigma}{\mathrm{d}t\ \mathrm{d}q^2\ \mathrm{d}\cos\theta_\ell^*}\bigg|_{\Delta_T=0} \\ &= \frac{8}{3}\ K\ \frac{1}{s - 4M^2}\ \frac{1}{(q^2)^5}\,. \end{aligned} \tag{A.6}$$

The integration of this equation in the two-dimensional bin $(\Delta q^2, \Delta \cos\theta_{\pi^0})$ defined by the limits $q_1^2 < q^2 < q_2^2$ and $\cos\theta_1 < \cos\theta_{\pi^0} < 1$ is done by first mapping the $\cos\theta$ boundaries to the ($q^2$ dependent) $t$ boundaries as given by eq. (A.5): $\cos\theta_1 < \cos\theta < 1 \Rightarrow t_{\mathrm{cut}}(q^2) < t < t_{\max}(q^2)$, with $t_{\mathrm{cut}}(q^2) \equiv t(\cos\theta_1, q^2)$ and $t_{\max}(q^2) \equiv t(1, q^2)$. Extrapolating the differential cross section (A.6) (obtained at $\cos\theta_{\pi^0} = 1$) to the angular region $\cos\theta_1 < \cos\theta_{\pi^0} < 1$, the integration in the two-dimensional bin $(\Delta q^2, \Delta \cos\theta_{\pi^0})$ is done as

$$\begin{aligned} \sigma &= \int_{q_1^2}^{q_2^2} \mathrm{d}q^2 \int_{t_{\mathrm{cut}}(q^2)}^{t_{\max}(q^2)} \mathrm{d}t\ \frac{\mathrm{d}\sigma}{\mathrm{d}q^2\ \mathrm{d}t}\bigg|_{\Delta_T=0} \\ &= \frac{8}{3}\ K\ \frac{1}{s - 4M^2}\ \int_{q_1^2}^{q_2^2} \mathrm{d}q^2\ \frac{1}{(q^2)^5}\big[t_{\max}(q^2) - t_{\mathrm{cut}}(q^2)\big]. \end{aligned} \tag{A.7}$$

For the estimates used in this analysis, the $q^2$ integration in eq. (A.7) has been done numerically.

## Appendix B. Background subtraction

In this appendix we describe the background subtraction procedure carried out in our analysis. For the clarity of the notation, we will refer to the signal channel $\bar{p}p \to e^+e^-\pi^0$ with the subscript $S$, and we will refer to the background channel $\bar{p}p \to \pi^+\pi^-\pi^0$ with the subscript $B$. In a data sample with luminosity $\mathcal{L}$, the expected number of signal and background events produced in an experiment is $N_S = \sigma_S\ \mathcal{L}$ and $N_B = \sigma_B\ \mathcal{L}$. After the event selection procedure, the expected number of reconstructed signal and background events becomes $N_S^R = \epsilon_S\ \sigma_S\ \mathcal{L}$ and $N_B^R = \epsilon_B\ \sigma_B\ \mathcal{L}$, where $\epsilon_S$ and $\epsilon_B$ are the reconstruction efficiencies for the signal and background channels. We remark that due to the high background suppression, $\epsilon_B$ is understood as an upper limit for the background reconstruction efficiency estimated at some confidence level, as discussed in sect. 7. Consequently, $N_B^R$ is also understood as an upper limit for background contamination, estimated at the same confidence level. The total number of observed events in the sample used for the measurement is therefore $N^R = N_S^R + N_B^R$, for which we assume a Poisson distribution with standard deviation $\Delta N^R = \sqrt{N^R}$. The estimation of the number of signal events in this sample is then done by subtracting the remaining background

contamination, and assuming standard error propagation:

$$N_S^R = N^R - N_B^R, \quad (\Delta N_S^R)^2 = (\Delta N^R)^2 + (\Delta N_B^R)^2. \quad \text{(B.1)}$$

The estimation of the background contamination $N_B^R = \epsilon_B\ \sigma_B\ \mathcal{L}$ requires the knowledge of the cross section $\sigma_B$, which can be measured with $\bar{\text{P}}$ANDA. In our analysis, however, we simply assume the relation $\sigma_B = 10^6\ \sigma_S$. The computation of the standard deviation is also determined by simple error propagation, according to

$$\left(\frac{\Delta N_B^R}{N_B^R}\right)^2 = \left(\frac{\Delta \epsilon_B}{\epsilon_B}\right)^2 + \left(\frac{\Delta \sigma_B}{\sigma_B}\right)^2. \quad \text{(B.2)}$$

Relying of the fact that the cross section corresponding to three-pion production from $\bar{p}p$ annihilation will be measured at $\bar{\text{P}}$ANDA with great precision due to its high statistics, we have neglected the last term $\Delta\sigma_B/\sigma_B$ in our analysis.

## References


1. S. Boffi, B. Pasquini, Riv. Nuovo Cimento **30**, 387 (2007).
2. L.L. Frankfurt, P.V. Pobylitsa, M.V. Polyakov, M. Strikman, Phys. Rev. D **60**, 014010 (1999).
3. B. Pire, L. Szymanowski, Phys. Rev. D **71**, 111501 (2005).
4. J.P. Lansberg, B. Pire, L. Szymanowski, Phys. Rev. D **75**, 074004 (2007) **77**, 019902(E) (2008).
5. J.P. Lansberg, B. Pire, K. Semenov-Tian-Shansky, L. Szymanowski, Phys. Rev. D **85**, 054021 (2012).
6. A. Kubarovskiy, AIP Conf. Proc. **1560**, 576 (2013).
7. $\bar{\text{P}}$ANDA Collaboration (M.F.M. Lutz *et al.*), *Physics Performance Report for $\bar{P}$ANDA: Strong Interaction Studies with Antiprotons*, arXiv:0903.3905 [hep-ex].
8. U. Wiedner, Prog. Part. Nucl. Phys. **66**, 477 (2011).
9. M. Sudol, M.C. Mora Espí *et al.*, Eur. Phys. J. A **44**, 373 (2010).
10. G.P. Lepage, S.J. Brodsky, Phys. Rev. D **22**, 2157 (1980).
11. V.L. Chernyak, A.R. Zhitnitsky, Phys. Rep. **112**, 173 (1984).
12. B. Pire, L. Szymanowski, Phys. Lett. B **622**, 83 (2005).
13. J.P. Lansberg, B. Pire, L. Szymanowski, Phys. Rev. D **76**, 111502 (2007).
14. J.P. Lansberg, B. Pire, K. Semenov-Tian-Shansky, L. Szymanowski, Phys. Rev. D **86**, 114033 (2012).
15. B. Pire, K. Semenov-Tian-Shansky, L. Szymanowski, Few-Body Syst. **55**, 351 (2014).
16. B. Pire, K. Semenov-Tian-Shansky, L. Szymanowski, Phys. Lett. B **724**, 99 (2013).
17. B. Ma, B. Pire, K. Semenov-Tian-Shansky, L. Szymanowski, *$\pi N$ TDAs from charmonium production in association with a forward pion at $\bar{P}$ANDA*, arXiv:1402.0413 [hep-ph].
18. B. Ma, *Simulation of electromagnetic channels for PANDA@FAIR*, PhD thesis, Université Paris-Sud, Orsay, France (2014).
19. C. Adamuscin, E.A. Kuraev, E. Tomasi-Gustafsson, F.E. Maas, Phys. Rev. C **75**, 045205 (2007).
20. J. Guttmann, M. Vanderhaeghen, Phys. Lett. B **719**, 136 (2013).
21. J. Boucher, *Feasibility studies of the $\bar{p}p \to e^+e^-\pi^0$ electromagnetic channel at $\bar{P}$ANDA*, PhD thesis, Institut für Physik, Mathematik und Informatik, Johannes Gutenberg Universität Mainz jointly with Institut de Physique Nucleaire d'Orsay, Université Paris-Sud, UMR 8608, CNRS-IN2P3, Orsay, France (2011).
22. M.C. Mora Espí, *Feasibility studies for accessing nucleon structure observables with the PANDA experiment at the future FAIR facility*, PhD thesis, Institut für Kernphysik, Johannes Gutenberg Universität, Mainz, Germany (2012).
23. GEANT4 Collaboration (S. Agostinelli *et al.*), Nucl. Instrum. Methods A **506**, 250 (2003).
24. K. Föhl *et al.*, Nucl. Instrum. Methods A **595**, 88 (2008).
25. M. Born, E. Wolf, *Principles of Optics* (Pergamon Oxford, 1970).
26. PANDA Collaboration (W. Erni *et al.*), Eur. Phys. J. A **49**, 25 (2013).
27. S. Banerjee, D.N. Brown, C. Chen, D. Cote, G.P. Dubois-Felsmann, I. Gaponenko, P.C. Kim, W.S. Lockman *et al.*, J. Phys. Conf. Ser. **119**, 032007 (2008).
28. B. Pire, K. Semenov-Tian-Shansky, L. Szymanowski, Phys. Rev. D **84**, 074014 (2011).
29. N.G. Stefanis, EPJ direct **7**, 1 (1991).
30. V.L. Chernyak, A.A. Ogloblin, I.R. Zhitnitsky, Z. Phys. C **42**, 583 (1989).
31. M. Pelizaeus, unpublished (2009).
32. A. Ryd, D. Lange, N. Kuznetsova, S. Versille, M. Rotondo, D.P. Kirkby, F.K. Wuerthwein, A. Ishikawa, *EvtGen: A Monte Carlo Generator for B-Physics*, EVTGEN-V00-11-07.
33. E. Barberio, Z. Was, Comput. Phys. Commun. **79**, 291 (1994).
34. T.C. Bacon, I. Butterworth, R.J. Miller, J.J. Phelan, R.A. Donald, D.N. Edwards, D. Howard, R.S. Moore, Phys. Rev. D **7**, 577 (1973).
35. O. Czyzewski *et al.*, in *Proceedings of the Sienna International Conference on Elementary Particles*, edited by G. Bernardini, G.P. Puppi (Società Italiana di Fisica, Bologna, Italy, 1963) p. 271 (also available as CERN/TC/PHYSICS 63-34).
36. D. Everett, P. Grossmann, P. Mason, H. Muirhead, Nucl. Phys. B **73**, 449 (1974).
37. F. Sai, S. Sakamoto, S.S. Yamamoto, Nucl. Phys. B **213**, 371 (1983).
38. Crystal Barrel Collaboration (A. Abele *et al.*), Phys. Lett. B **469**, 270 (1999).
39. J. Van de Wiele, S. Ong, Eur. Phys. J. A **46**, 291 (2010).
40. A. Galoian, V.V. Uzhinsky, AIP Conf. Proc. **796**, 79 (2005).
41. V. Flaminio, W.G. Moorhead, D.R.O. Morrision, N. Rivoire, *Compilation of cross sections III: p and $\bar{p}$ induced reactions*, CERN-HERA 84-01.
42. Particle Data Group (K.A. Olive *et al.*), Chin. Phys. C **38**, 090001 (2014).
43. J.C. Collins, L. Frankfurt, M. Strikman, Phys. Rev. D **56**, 2982 (1997).
44. T. Horn, X. Qian, J. Arrington, R. Asaturyan, F. Benmokthar, W. Boeglin, P. Bosted, A. Bruell *et al.*, Phys. Rev. C **78**, 058201 (2008).
45. E. Fuchey, A. Camsonne, C. Munoz Camacho, M. Mazouz, G. Gavalian, E. Kuchina, M. Amarian, K.A. Aniol *et al.*, Phys. Rev. C **83**, 025201 (2011).

46. CLAS Collaboration (I. Bedlinskiy *et al.*), *Exclusive $\pi^0$ electroproduction at $W > 2\,\mathrm{GeV}$ with CLAS*, arXiv:1405.0988 [nucl-ex].
47. T. Ullrich, Z. Xu, *Treatment of Errors in Efficiency Calculations* (2008) arXiv:physics/0701199 [physics.data-an].
48. B. Pire, K. Semenov-Tian-Shansky, L. Szymanowski, Phys. Rev. D **82**, 094030 (2010).
49. B. Pasquini, M. Pincetti, S. Boffi, Phys. Rev. D **80**, 014017 (2009).
50. A.T. Goritschnig, B. Pire, W. Schweiger, Phys. Rev. D **87**, 014017 (2013).